INL/JOU-25-85137-Revision-1

Enabling Grid-Forming Control with Fault Ride-Through in Unbalanced Distribution Networks

January 2026

Yemi Ojo, Soumyadeep Nag, Temitayo Olayemi Olowu

Changing the World's Energy Future

INL is a U.S. Department of Energy National Laboratory operated by Battelle Energy Alliance, LLC

INL/JOU-25-85137-Revision-1

Enabling Grid-Forming Control with Fault Ride-Through in Unbalanced Distribution Networks

Yemi Ojo, Soumyadeep Nag, Temitayo Olayemi Olowu

January 2026

Idaho National Laboratory
Idaho Falls, Idaho 83415

http://www.inl.gov

Prepared for the
U.S. Department of Energy
Under DOE Idaho Operations Office
Contract DE-AC07-05ID14517

Enabling Grid-Forming Control with Fault Ride-Through in Unbalanced Distribution Networks

Yemi Ojo, Soumyadeep Nag, and Temitayo O. Olowu

***Abstract*— Distribution networks are often unbalanced, causing oscillatory responses in inverter control designed for balanced conditions. To address this problem, this paper proposes a novel time-domain transformation appropriate for inverter control and enables the decomposition of three-phase unbalanced signals into constant positive and negative components. Relations useful for calculating unbalanced active and reactive power are derived from first principle, providing insight into vector products of unbalanced three-phase signals. Furthermore, a grid-forming control effective under unbalanced conditions is developed, which delivers superior performance while meeting UNIFI specifications applicable to category 4 inverter-based resource, like setting and regulating frequency/voltage, providing voltage support, sharing active power, injecting negative sequence current, and riding through faults. A current limiter is proposed for safe fault ride-through and integrates with the grid-forming control featuring frequency/voltage droop controllers and current and voltage control loops. The transformation of interconnected inverters is formulated and stability of the proposed control analyzed to support robust parameter selections. The effectiveness of the proposed transformation and grid-forming control is demonstrated through analytical results and real-time simulation of a IEEE 123 distribution network on the Real-Time Digital Simulator. Comparison with existing methods shows that the proposed strategy satisfies the UNIFI specifications with a much better performance.**

***Index Terms*— Distribution networks, grid-forming control, three-phase inverters, unbalanced three-phase signals, stability**

I. Introduction

Incidents like the April 2025 Spain and Portugal blackout highlight the need to enhance grid resilience globally [1]. One possible solution is enabling grid-forming capabilities in distribution networks, considering their rapid penetration by inverter-based resources. Power generation from inverter-based resources is projected to be about 900 GW by 2031 [2]. Distribution networks with inverter-based resources can bring generation close to demand, thereby improving flexibility, power quality, and delivery of power to critical loads.

A. Literature Review

Distribution networks, including low and medium voltage microgrids, are often unbalanced due to uneven loading across the three phases and occurrences of unbalanced faults. Effective control policies are essential, as inverters and their functionalities can play significant roles in maintaining the stability and reliability of distribution networks. Globally, most inverter-based resources connected to grids employ grid-following control, where synchronization is achieved through phase lock loops and predefined amount of active and reactive power [3] are injected. Nonetheless, grid-following inverters cannot set and regulate grid frequency and voltage, and studies have shown that grids with high penetration of these resources often experience instability and reliability issues, especially during grid disruptions and failures [4, 5]. As a result, there has been a growing demand to reinforce grids with grid-forming inverters [6], which can set and maintain grid frequency and voltage similarly to synchronous generators, and with appropriate design, can mitigate the impact of imbalances in distribution networks. Various grid-forming control strategies have been proposed, including current and active power-based droop control, angle droop control, virtual synchronous machine control [7]–[11], and virtual impedance techniques [12]. These strategies can be incorporated with single loop voltage control or double nested control loops [7, 8, 10].

These grid-forming control, while providing active power sharing and frequency and voltage regulation, assume balanced grid conditions which is often not the case in distribution networks. Under unbalanced conditions, these schemes give oscillatory responses, a drawback due to the direct-quadrature (dq) signals oscillating at frequency twice the synchronous frequency [3]. For context, due to the continuous variation of the amplitude of sinusoidal signals, it is convenient to first transform these signals into constant dq quantities before implementing inverter control. Under balanced conditions, this transformation can be achieved using the standard Park-Clarke $dq0-$transformation [13]. This is however not the case under unbalanced conditions where the $dq0-$transformation produces yet again another sinusoidal signal that oscillates at frequency twice the synchronous frequency [3], thus complicating grid-forming control design. Although low-pass filters can remove these oscillations, they slow down controller response during transients [3, 14]–[17].

Grid-forming control tailored for unbalanced operations exist in the literature. These are predominantly of two types. The first approach utilizes proportional resonant (PR) controllers in the stationary $\alpha\beta$ reference frame [3, 14, 18]. Although low-pass filters may not be required, its design for a particular frequency can render it less adaptive under large frequency deviations. The second approach utilizes formulations in the Double-Decoupled Synchronous Reference Frame (DDSRF), which employs separate dq frames for the

The authors are with Idaho National Laboratory (INL), Idaho Falls, USA. Emails: {yemi.ojo, soumyadeep.nag, temitayo.olowu}@inl.gov. This work is supported through the INL Laboratory Directed Research and Development (LDRD) Program under DOE Idaho Operations Office Contract DE-AC07-05ID14517. Made use of INL's High Performance Computing systems located at the Collaborative Computing Center and supported by the Office of Nuclear Energy of the U.S. Department of Energy and the Nuclear Science User Facilities under Contract No. DE-AC07-05ID14517.

positive and negative sequence components [3, 15]–[17]. This approach requires low-pass filters, which can lead to slow controller responses. Also the transformation employed are often not represented in a form that eases control design and analysis [3, 15]–[17]. Another aspect is the response of existing grid-forming control under unbalanced faults, which have been understudied. Limiting current under unbalanced faults is generally challenging because grid-forming controllers set and regulate grid frequency and voltage. Existing solutions includes injecting positive sequence current for fault ride-through, but negative sequence voltage is not mitigated [19, 20]. Strategies relying on online impedance estimation exist [21]. Saturation units have been used on both positive and negative sequence voltages [22, 23], though may suffer from integrator wind-up and cause instability [24].

Recent works on unbalanced grid-forming control adopt PR with systematic parameter design [14, 25], while others combine grid-feeding strategies for voltage support [21]. The latter relies on online impedance estimations and due to PR both schemes can suffer under frequency variations. Another employs signal resolvers to address imbalances, though built with fault limiters the resolver structure uses DDSRF [17]. In another approach, a decoupling grid-forming control leverages distribution network properties to enhance frequency/voltage regulation, but traditional dq transformation have been used [26]. Control architecture focused on balanced faults has been explored [27]–[29], but has limited application under unbalanced faults. A grid-forming control using balancing feedback has been proposed, but may have trade-off imbalances between voltage and power [30]. Virtual oscillator-based designs incorporate current limiting but are often highly nonlinear [31, 32]. The new UNIFI[1] specifications for grid-forming control under unbalanced conditions outlined frequency/voltage regulation, active power sharing, voltage support provision, negative sequence current injection, and fault ride-through requirements [33]. Although existing strategies implicitly address most of these criteria, control design providing insight on satisfying all the requirements would be of practical relevance. Moreover, strategies satisfying the requirements with better performance are desired.

B. Paper Contributions

To address the drawbacks highlighted above, this paper proposes a novel time-domain transformation and grid-forming control that is effective under unbalanced conditions and is formulated in the positive and negative dq reference frame. The transformation is unique by its ability to convert unbalanced three-phase signals into constant positive and negative dq components without requiring the use of low-pass filters. It also facilitates the derivation of relations useful for calculating active and reactive power for unbalanced conditions. The grid-forming control is distinctive by its ability to deliver superior performance while satisfying UNIFI specifications [33] like setting and regulating frequency and voltage, sharing active power, providing voltage support, injecting negative sequence current, and riding through faults. The proposed strategy differs from existing solutions. Unlike DDSRF methods [3, 15]–[17], the time-domain transformation generates ripple-free signals without the use of low-pass filters, thus enabling quick response in the proposed control. Contrary to PR controllers [3, 14, 18, 25], the proposed transformation is robust to frequency variations. The orientation of its positive and negative dq components supports grid-forming control design, as opposed to [34]. Contrary to complex approaches in [3, 15]–[18, 31, 32], the proposed control has a simple implementation and is effective under unbalanced conditions, and the proposed transformation has a concise form that eases control design and analysis. The proposed control provides voltage support by injecting both positive and negative sequence currents and can handle unbalanced faults, in contrast to [19, 20, 27]–[29]. The proposed current limiter uniformly restricts positive and negative sequence current during fault, avoids saturation units which can cause integrator wind-up [24], and incorporates a feature that in contrast to [14] it prevents excessive restriction during fault. Moreover, through the proposed approach insight is provided on satisfying the UNIFI specifications.

The main contributions of this paper are summarized as follows.

1) A time-domain transformation is proposed, suitable for inverter control and enables the conversion of unbalanced three-phase signals into constant positive and negative components without requiring low-pass filters.
2) Relations crucial for calculating unbalanced active and reactive power are derived from first principles, providing insight on the vector product of unbalanced three-phase signals.
3) A grid-forming control utilizing the transformation and effective under unbalanced conditions is proposed, with a much better performance while meeting UNIFI specifications like setting and regulating frequency and voltage, sharing active power, providing voltage support, injecting negative sequence current, and riding through faults.
4) A current limiter is proposed that ensures safe fault ride-through and integrates with the grid-forming control featuring frequency and voltage droops and current and voltage control loops.
5) Transformation of interconnected inverters is formulated and stability of the proposed control investigated to facilitate robust parameters selections.

Furthermore, the effectiveness of the proposed transformation and grid-forming control is validated by analytical results and full-order EMT real-time simulation conducted on a modified IEEE 123 distribution network using the Real-Time Digital Simulator (RTDS). A comparative study with DDSRF and PR methods is also presented.

[1]UNIFI: UNiversal Interoperability for grid-Forming Inverters [33] – states specifications for grid-forming control under unbalanced conditions.

C. Paper Outline

The remainder of the paper is organized as follows. Section II presents the coordinate transformation and derivation of power relations. Section III discusses the proposed grid-forming control. The transformation of interconnected inverters and stability analysis are presented in Section IV. Real-time simulations and comparative studies are conducted in Section V, and conclusions are given in Section VI.

D. Notation

Let $\mathbb{R}_{>0}$ ($\mathbb{R}_{\geq 0}$) be a set of real numbers greater than (greater than or equal to) 0 and $\mathbb{S} = [0, 2\pi)$. Let $\mathbf{1}_n$ ($\mathbf{0}_n$) denote an n-dimensional column vector of ones (zeros). $\mathbf{0}_{n\times m}$ is an $n \times m$ zero matrix and $\mathbf{I}_n$ as the identity matrix of size n. Let $\text{col}(x_i) \in \mathbb{R}^n$ denote a column vector with entries $x_i \in \mathbb{R}$, $\text{diag}(a_i) \in \mathbb{R}^{n\times n}$ an $n \times n$ diagonal matrix with diagonal entries $a_i \in \mathbb{R}^n$, and $\otimes$ denotes a Kronecker product. The time argument t will often be omitted in the text for convenience in the presentation.

II. Coordinate Transformation of Unbalanced Three-Phase Signals

This section presents a time-domain transformation that enables decomposition of unbalanced electrical signals and into positive and negative synchronous reference frames. To this end, consider a generic three-phase electrical system represented by the model

$$\dot{x}_{abc}(t) = f(x_{abc}(t)) \tag{1}$$

where $t \in \mathbb{R}_{\geq 0}$, and the state vector, $x_{abc}(t) \in \mathbb{R}^3$, denotes unbalanced asymmetric three-phase signals described by

$$x_{abc}(t) = \sqrt{2}\begin{bmatrix} X_a \sin(\theta(t) + \phi_a) \\ X_b \sin(\theta(t) + \phi_b - \frac{2\pi}{3}) \\ X_c \sin(\theta(t) + \phi_c + \frac{2\pi}{3}) \end{bmatrix} \tag{2}$$

where $\phi_a, \phi_b, \phi_c \in \mathbb{R}_{\geq 0}$ are constant phase shifts, and $X_a, X_b, X_c \in \mathbb{R}_{\geq 0}$ are the three-phase RMS values, respectively. Note that the three-phase waveform (2) represents the general case where $X_a \neq X_b \neq X_c$ and $\phi_a \neq \phi_b \neq \phi_c$. $\theta(t) \in \mathbb{S}$ is the phase angle and oscillates with frequency, $\omega(t) \in \mathbb{R}_{\geq 0}$, as follows

$$\dot{\theta}(t) = \omega(t). \tag{3}$$

Let $\tau = 1/4f$ where $f = \omega/2\pi \in \mathbb{R}_{\geq 0}$ is the frequency of the unbalanced three-phase signal $x_{abc}(t)$. Then, $x_{abc}(t-\tau)$ is used to denote the signal $x_{abc}(t)$ delayed[2] by τ.

A. Employed Coordinate Transformation

This section presents the coordinate transformation employed in this paper to decompose unbalanced three-phase signals, $x_{abc}(t)$, into non-oscillatory positive and negative dq components. To this end, consider the standard Clarke ($\alpha\beta\gamma$) and Park ($dq0$) transformation matrices

$$T_{\alpha\beta\gamma} = \sqrt{\frac{2}{3}}\begin{bmatrix} 1 & -\frac{1}{2} & -\frac{1}{2} \\ 0 & \frac{\sqrt{3}}{2} & -\frac{\sqrt{3}}{2} \\ \frac{1}{\sqrt{2}} & \frac{1}{\sqrt{2}} & \frac{1}{\sqrt{2}} \end{bmatrix}, \tag{4}$$

$$T_{dq0}(\cdot) = \begin{bmatrix} \cos(\cdot) & \sin(\cdot) & 0 \\ -\sin(\cdot) & \cos(\cdot) & 0 \\ 0 & 0 & 1 \end{bmatrix}, \tag{5}$$

where $T_{\alpha\beta\gamma}$, $T_{dq0}(\cdot)$ are orthogonal matrices (i.e., $T^{-1}_{\alpha\beta\gamma} = T^{\top}_{\alpha\beta\gamma}$ and $T^{-1}_{dq0} = T^{\top}_{dq0}$).

To support grid-forming control design purposes, we seek to align phase a with the d axis, unlike the orientation in [34]. In this paper, this is achieved by performing a clockwise $\pi/2$ rotation of the $dq0$ transformation matrix (5), as follows

$$\tilde{T}_{dq0}(\cdot) = T_{dq0}(-\frac{\pi}{2})\, T_{dq0}(\cdot) = \begin{bmatrix} \sin(\cdot) & -\cos(\cdot) & 0 \\ \cos(\cdot) & \sin(\cdot) & 0 \\ 0 & 0 & 1 \end{bmatrix}. \tag{6}$$

The transformation matrix employed in this paper for the coordinate transformation is given by

$$T(t) = \hat{T}_{dq0}(t) T_{+-0} \hat{T}_{\alpha\beta\gamma} \tag{7}$$

where

$$\hat{T}_{\alpha\beta\gamma} = \begin{bmatrix} T_{\alpha\beta\gamma} & \mathbf{0}_{3\times 3} \\ \mathbf{0}_{3\times 3} & T_{\alpha\beta\gamma} \end{bmatrix}, \tag{8}$$

$$\hat{T}_{dq0}(t) = \begin{bmatrix} \tilde{T}_{dq0}(\theta(t)) & \mathbf{0}_{3\times 3} \\ \mathbf{0}_{3\times 3} & \tilde{T}_{dq0}(-\theta(t)) \end{bmatrix}, \tag{9}$$

$$T_{+-0} = \frac{1}{2}\begin{bmatrix} 1 & 0 & 0 & 0 & -1 & 0 \\ 0 & 1 & 0 & 1 & 0 & 0 \\ 0 & 0 & 1 & 0 & 0 & 0 \\ 1 & 0 & 0 & 0 & 1 & 0 \\ 0 & 1 & 0 & -1 & 0 & 0 \\ 0 & 0 & 0 & 0 & 0 & 1 \end{bmatrix}, \tag{10}$$

and $T(t), \hat{T}_{\alpha\beta\gamma}, \hat{T}_{dq0}(t), T_{+-0} \in \mathbb{R}^{6\times 6}$. The matrix, T_{+-0}, performs signal cancellation, as generated from the delayed signal cancellation method [34, 35]. Noting that T_{+-0} is full rank and $\hat{T}_{\alpha\beta\gamma}$, $\hat{T}_{dq0}(t)$ are orthogonal matrices (i.e., $\hat{T}^{\top}_{\alpha\beta\gamma}\hat{T}_{\alpha\beta\gamma} = \mathbf{I}_6$, $\hat{T}^{\top}_{dq0}(t)\hat{T}_{dq0}(t) = \mathbf{I}_6$), then the inverse of matrix, T_{+-0}, exists and is given by

$$T^{-1}(t) = \hat{T}^{\top}_{\alpha\beta\gamma} T^{-1}_{+-0} \hat{T}^{\top}_{dq0}(t). \tag{11}$$

Then, the time-domain coordinate transformation employed in this paper is given by

$$x^{+-}_{dq0}(t) = \begin{bmatrix} x^{+}_{dq0}(t) \\ x^{-}_{dq0}(t) \end{bmatrix} = T(t)\begin{bmatrix} x_{abc}(t) \\ x_{abc}(t-\tau) \end{bmatrix} \tag{12}$$

where the signals

$$\begin{aligned} x^{+}_{dq0}(t) &= \begin{bmatrix} x^{+}_{d}(t) & x^{+}_{q}(t) & x^{+}_{0}(t) \end{bmatrix}^{\top} \\ x^{-}_{dq0}(t) &= \begin{bmatrix} x^{-}_{d}(t) & x^{-}_{q}(t) & x^{-}_{0}(t) \end{bmatrix}^{\top} \end{aligned} \tag{13}$$

denote the $dq0$ positive and negative components which

[2]Note that a time delay of $\tau = 1/4f$ produces a phase delay of $\pi/2$ since for every period $1/f$ there is a complete phase revolution 2π. Thus, delaying $x_{abc}(t)$ by τ means delaying the phase angle of $x_{abc}(t)$ by $\pi/2$.

rotate with $\theta(t)$ and $-\theta(t)$, respectively. Rewriting $T^{-1}(t)$ in (11) as

$$T^{-1}(t) = \begin{bmatrix} \mathcal{T}_t(t) \\ \mathcal{T}_\tau(t) \end{bmatrix}, \tag{14}$$

where $\mathcal{T}_t(t), \mathcal{T}_\tau(t) \in \mathbb{R}^{3\times 6}$, then the inverse of the employed coordinate transformation is given by

$$\begin{aligned} x_{abc}(t) &= \mathcal{T}_t(t) x^{+-}_{dq0}(t), \\ x_{abc}(t-\tau) &= \mathcal{T}_\tau(t) x^{+-}_{dq0}(t). \end{aligned} \tag{15}$$

According to (7), the employed coordinate transformation in (12) involves three steps. First, the unbalanced three-phase signals, $x_{abc}(t), x_{abc}(t-\tau)$, are transformed into the $\alpha\beta\gamma$ components using the standard Clarke transformation (8). Second, the $\alpha\beta\gamma$ components are processed through the delay signal cancellation transformation (10), leading to the resulting signals being converted into the positive and negative $dq0$ components using the $dq0$ transformation (9).

To illustrate the benefit of the transformation (7), the explicit expression of (12) is obtained, as follows:

$$\begin{aligned} x^{+-}_{dq0}(t) &= T(t) \begin{bmatrix} x_{abc}(t) \\ x_{abc}(t-\tau) \end{bmatrix} \\ &= \begin{bmatrix} x^+_d & x^+_q & x^+_0 & x^-_d & x^-_q & x^-_0 \end{bmatrix}^\top \end{aligned} \tag{16}$$

where

$$x^+_d = \frac{1}{\sqrt{3}}(X_a \cos\phi_a + X_b \cos\phi_b + X_c \cos\phi_c) \tag{17a}$$

$$x^+_q = \frac{1}{\sqrt{3}}(X_a \sin\phi_a + X_b \sin\phi_b + X_c \sin\phi_c) \tag{17b}$$

$$\begin{aligned} x^+_0 = {} & \frac{1}{2\sqrt{6}}\left[2X_a \sin(\theta(t)+\phi_a) - X_b \sin(\theta(t)+\phi_b)\right. \\ & \left. - X_c \sin(\theta(t)+\phi_c)\right] + \frac{1}{2\sqrt{2}}\left[-X_b \cos(\theta(t)+\phi_b)\right. \\ & \left. + X_c \cos(\theta(t)+\phi_c)\right] \end{aligned} \tag{17c}$$

$$\begin{aligned} x^-_d = {} & \frac{1}{2\sqrt{3}}(-2X_a \cos\phi_a + X_b \cos\phi_b + X_c \cos\phi_c) \\ & + \frac{1}{2}(X_b \sin\phi_b - X_c \sin\phi_c) \end{aligned} \tag{17d}$$

$$\begin{aligned} x^-_q = {} & \frac{1}{2\sqrt{3}}(2X_a \sin\phi_a - X_b \sin\phi_b - X_c \sin\phi_c) \\ & + \frac{1}{2}(X_b \cos\phi_b - X_c \cos\phi_c) \end{aligned} \tag{17e}$$

$$\begin{aligned} x^-_0 = {} & \frac{1}{2\sqrt{6}}\left[-2X_a \cos(\theta(t)+\phi_a) + X_b \cos(\theta(t)+\phi_b)\right. \\ & \left. + X_c \cos(\theta(t)+\phi_c)\right] + \frac{1}{2\sqrt{2}}\left[-X_b \sin(\theta(t)+\phi_b)\right. \\ & \left. + X_c \sin(\theta(t)+\phi_c)\right] \end{aligned} \tag{17f}$$

Evidently, the positive and negative components, $x^+_d, x^+_q, x^-_d, x^-_q$, are constant signals at steady state due to constant phase shifts ϕ_a, ϕ_b, ϕ_c and RMS values, X_a, X_b, X_c, while the zero components, x^+_0, x^-_0, oscillate with frequency, ω. This indicates the advantage of the coordinate transformation (12) over the standard Park-Clarke transformation, which produces oscillatory dq components under imbalances. Unlike DDSRF methods [3, 15]–[17], the transformation (12) enables the generation of positive and negative signals, $x^+_d, x^+_q, x^-_d, x^-_q$, that eliminate the need for low-pass filters. Considering (17), the same benefit applies if:

(i) $x_{abc}(t)$ is unbalanced and symmetric, i.e., $X_a \neq X_b \neq X_c$ and $\phi_a = \phi_b = \phi_c = \phi$.
(ii) $x_{abc}(t)$ is unbalanced and symmetric with zero phase shifts, i.e., $X_a \neq X_b \neq X_c$ and $\phi_a = \phi_b = \phi_c = 0$.
(iii) $x_{abc}(t)$ is balanced and asymmetric, i.e., $X_a = X_b = X_c$ and $\phi_a \neq \phi_b \neq \phi_c$.
(iv) $x_{abc}(t)$ is balanced and symmetric, i.e., $X_a = X_b = X_c$ and $\phi_a = \phi_b = \phi_c = \phi$.
(v) $x_{abc}(t)$ is balanced and symmetric with zero phase shifts, i.e., $X_a = X_b = X_c$ and $\phi_a = \phi_b = \phi_c = 0$.

Cases (iv) and (v) show that the $x^+_0, x^-_d, x^-_q, x^-_0$ in (16)–(17) are zero, thus allowing to recover the standard $dq0$ transformation under balanced and symmetric conditions (see e.g., [3]). Furthermore, note that the phase shifts ϕ_a, ϕ_b, ϕ_c are generally small. Thus, by (17) x^+_d is considerably larger than x^+_q, and implies that the d axis aligns with phase a, a property incorporated into (7) by the modified dq transform (6). This is appropriate for grid-forming control where the inverter output voltage (positive) d-component is often controlled so that its value matches the desired voltage magnitude (see e.g., [7, 8]).

B. Associated Properties of Employed Transformation

This section presents results on the vector product of unbalanced three-phase signals and facilitates deriving from first principles relations for unbalanced active and reactive power. These are stated in Theorems 1 and 2 below. To this end, first we state Lemma 1.

Lemma 1: Consider (4), (18), and defining skew matrices

$$J = \begin{bmatrix} 0 & 1 \\ -1 & 0 \end{bmatrix}, \qquad H = \begin{bmatrix} 0 & 1 & -1 \\ -1 & 0 & 1 \\ 1 & -1 & 0 \end{bmatrix}. \tag{18}$$

Rewriting $\tilde{T}_{dq0}(\cdot)$ in (6) as

$$\tilde{T}_{dq0}(\cdot) = \begin{bmatrix} \mathcal{R}(\cdot) & \mathbf{0}_2 \\ \mathbf{0}_2^\top & 1 \end{bmatrix}, \ \mathcal{R}(\cdot) = \begin{bmatrix} \sin(\cdot) & -\cos(\cdot) \\ \cos(\cdot) & \sin(\cdot) \end{bmatrix}. \tag{19}$$

The following relations hold:

$$T_{\alpha\beta\gamma} H^\top T^\top_{\alpha\beta\gamma} = \begin{bmatrix} \sqrt{3}J^\top & \mathbf{0}_2 \\ \mathbf{0}_2^\top & 0 \end{bmatrix} \tag{20a}$$

$$\mathcal{R}(-\theta) = -\mathcal{R}^\top(\theta), \tag{20b}$$

$$\mathcal{R}(\theta)J^\top = J^\top \mathcal{R}(\theta), \ \mathcal{R}^\top(\theta)J^\top = J^\top \mathcal{R}^\top(\theta) \tag{20c}$$

$$\mathcal{R}^\top(\theta)\mathcal{R}(\theta) = \mathcal{R}(\theta)\mathcal{R}^\top(\theta) = \mathbf{I}_2 \tag{20d}$$

$$-\mathcal{R}(\theta)\mathcal{R}(\theta) = \begin{bmatrix} \cos 2(\theta) & \sin 2(\theta) \\ -\sin 2(\theta) & \cos 2(\theta) \end{bmatrix} \tag{20e}$$

Proof: The proof can be found in Appendix I. ■

Theorem 1: Consider (4), (6), (7), (10), (14), (18)–(20), and defining

$$\mathcal{T}_{11} = \begin{bmatrix} \mathbf{I}_2 & \mathbf{0}_2 \\ \mathbf{0}_2^\top & 2 \end{bmatrix}, \quad \mathcal{T}_{12} = \begin{bmatrix} \mathbf{I}_2 & \mathbf{0}_2 \\ \mathbf{0}_2^\top & 0 \end{bmatrix}. \tag{21}$$

Then, it holds that

$$\mathcal{T}_t = \begin{bmatrix} T_{\alpha\beta\gamma}^\top \mathcal{T}_{11} \tilde{T}_{dq0}^\top(\theta) & T_{\alpha\beta\gamma}^\top \mathcal{T}_{12} \tilde{T}_{dq0}^\top(-\theta) \end{bmatrix} \tag{22}$$

$$\mathcal{T}_t^\top \mathcal{T}_t = \begin{bmatrix} \mathbf{I}_2 & \mathbf{0}_2 & -\mathcal{R}(\theta)\mathcal{R}(\theta) & \mathbf{0}_2 \\ \mathbf{0}_2^\top & 4 & \mathbf{0}_2^\top & 0 \\ -\mathcal{R}^\top(\theta)\mathcal{R}^\top(\theta) & \mathbf{0}_2 & \mathbf{I}_2 & \mathbf{0}_2 \\ \mathbf{0}_2^\top & 0 & \mathbf{0}_2^\top & 0 \end{bmatrix} \tag{23}$$

$$\mathcal{T}_t^\top H^\top \mathcal{T}_t = \begin{bmatrix} \sqrt{3}J^\top & \mathbf{0}_2 & -\sqrt{3}J^\top \mathcal{R}(\theta)\mathcal{R}(\theta) & \mathbf{0}_2 \\ \mathbf{0}_2^\top & 0 & \mathbf{0}_2^\top & 0 \\ -\sqrt{3}J^\top \mathcal{R}^\top(\theta)\mathcal{R}^\top(\theta) & \mathbf{0}_2 & \sqrt{3}J^\top & \mathbf{0}_2 \\ \mathbf{0}_2^\top & 0 & \mathbf{0}_2^\top & 0 \end{bmatrix} \tag{24}$$

where $\mathcal{T}_t := \mathcal{T}_t(t) \in \mathbb{R}^{3\times 6}$; $\theta := \theta(t)$; $\mathcal{T}_t^\top \mathcal{T}_t := \mathcal{T}_t^\top(t)\mathcal{T}_t(t) \in \mathbb{R}^{6\times 6}$; and $\mathcal{T}_t^\top H^\top \mathcal{T}_t := \mathcal{T}_t^\top(t) H^\top \mathcal{T}_t(t) \in \mathbb{R}^{6\times 6}$.

Proof: The proof can be found in Appendix II. ■

Matrices (23)–(24) allow to perform the vector products of two unbalanced signals of waveform (2), leading to the derivation of unbalanced active and reactive from first principles. This result is stated in Theorem 2 below.

Theorem 2: Consider unbalanced three-phase signals $v_{o,abc}(t)$ and $i_{o,abc}(t)$ of waveform (2), and (15), (20), (23)–(24). Then, the vector products

$$v_{o,abc}^\top \, i_{o,abc} = v_{o,dq0}^{+-\top} \mathcal{T}_t^\top \mathcal{T}_t \, i_{o,dq0}^{+-} \tag{25}$$

$$\frac{1}{\sqrt{3}} v_{o,abc}^\top H i_{o,abc} = \frac{1}{\sqrt{3}} v_{o,dq0}^{+-\top} \mathcal{T}_t^\top H^\top \mathcal{T}_t \, i_{o,dq0}^{+-} \tag{26}$$

hold, and are equally

$$\begin{aligned} v_{o,abc}^\top \, i_{o,abc} = & \underbrace{v_{o,dq}^{+\top} i_{o,dq}^{+} + v_{o,dq}^{-\top} i_{o,dq}^{-}}_{avg_P} \\ & + (v_{o,dq}^{+\top} i_{o,dq}^{-} + v_{o,dq}^{-\top} i_{o,dq}^{+}) \cos(2\theta) + 4 v_{o,0}^{+} \, i_{o,0}^{+} \\ & + (v_{o,dq}^{+\top} J \, i_{o,dq}^{-} + v_{o,dq}^{-\top} J^\top \, i_{o,dq}^{+}) \sin(2\theta) \end{aligned} \tag{27}$$

$$\begin{aligned} \frac{1}{\sqrt{3}} v_{o,abc}^\top H^\top i_{o,abc} = & \underbrace{v_{o,dq}^{+\top} J^\top i_{o,dq}^{+} + v_{o,dq}^{-\top} J^\top i_{o,dq}^{-}}_{avg_Q} \\ & + (v_{o,dq}^{+\top} J^\top \, i_{o,dq}^{-} + v_{o,dq}^{-\top} J^\top \, i_{o,dq}^{+}) \cos(2\theta) \\ & + (v_{o,dq}^{+\top} \, i_{o,dq}^{-} - v_{o,dq}^{-\top} \, i_{o,dq}^{+}) \sin(2\theta). \end{aligned} \tag{28}$$

Proof: The proof can be found in Appendix III. ■

If $v_{o,abc}(t)$, $i_{o,abc}(t)$ represent voltage and current, respectively, then the vector products in (27)–(28) give the *active* and *reactive* power under unbalanced conditions. Since in (17) the positive and negative dq-components are non-oscillatory, the terms avg_P and avg_Q in (27)–(28) are non-oscillatory, which are referred to as the average active and reactive power, respectively. The remaining terms in (27)–(28) oscillate at twice the frequency, $\omega(t)$, causing active and reactive power to oscillate at twice the system frequency under unbalanced conditions. Under balanced conditions, the oscillatory terms and negative sequence products $v_{o,dq}^{-\top} i_{o,dq}^{-}$, $v_{o,dq}^{-\top} J^\top i_{o,dq}^{-}$ become zero, allowing to recover the standard dq active power and reactive relations (see e.g., [3, 7]).

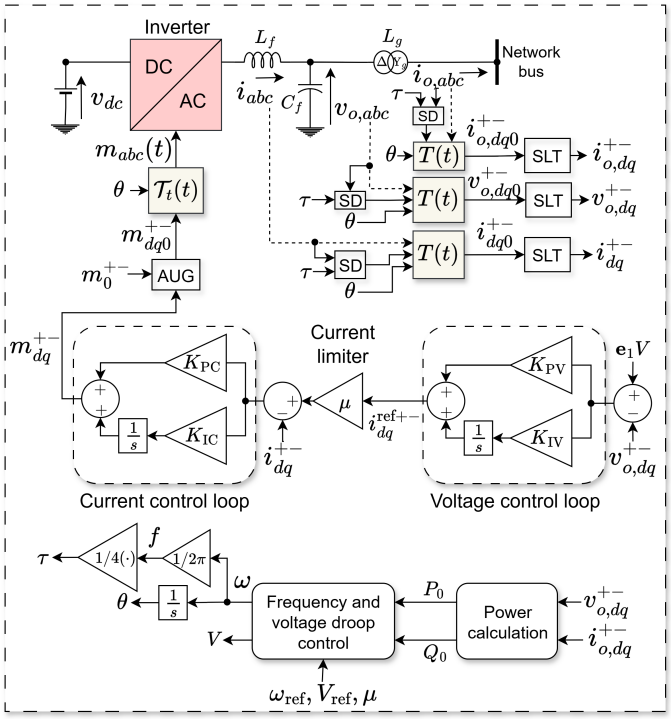

Fig. 1: Inverter circuit and proposed grid-forming control

III. Proposed Control

The aim in this paper is to propose a control design that provides insight on satisfying the UNIFI specifications applicable to inverter-based resource in category 4 [33]. To this end, a grid-forming control is designed that meets UNIFI specifications for grid-forming control under unbalanced conditions [33], such as:

S1- Setting and regulating frequency and voltage
S2- Sharing active power
S3- Providing voltage support
S4- Injecting negative sequence current
S5- Providing fault ride-through

Therefore, in this section the grid-forming control is developed to meet **S1**–**S5**. This is achieved through the control architecture which features enhanced frequency and voltage droop control and cascaded voltage and current control loops that are formulated in the positive and negative dq reference frame and seamlessly integrate with a current limiter.

To present the controllers featured in the grid-forming control, consider the inverter system (Fig. 1) which consists of the inverter circuit, signal transformation, and proposed control architecture. The AC-side of the inverter has an LC filter with inductance and capacitance, $L_f, C_f \in \mathbb{R}_{>0}$, respectively. The inverter may be connected to the grid via a Δ-Y_g transformer with inductance, $L_g \in \mathbb{R}_{>0}$, where the transformer Δ-winding traps the zero components [32]. The signals, $i_{abc}, i_{o,abc}, v_{o,abc} \in \mathbb{R}^3$, are of the form (2) and

are the inverter three-phase input and output currents and output voltage, respectively. $m_{abc} \in \mathbb{R}^3$ is the three-phase modulating signal also of the form (2). For completeness in the presentation, the abc system of inverter j is described by

$$\begin{aligned} L_{f_j}\,\dot{i}_{abc,j} &= -R_{f_j}\,i_{abc,j} + \frac{1}{2}v_{dc,j}m_{abc,j} - v_{o,abc,j} \\ C_{f_j}\,\dot{v}_{o,abc,j} &= i_{abc,j} - i_{o,abc,j} \end{aligned} \tag{29}$$

where $R_{f_j} \in \mathbb{R}_{\geq 0}$ is the parasitic part of the inductor L_{f_j}.

The grid-forming control is formulated in the positive and negative dq frame. To facilitate this, the three-phase signals, $i_{abc,j}, v_{o,abc,j}, i_{o,abc,j}$, are respectively, decomposed into $i^{+-}_{dq0,j}, v^{+-}_{o,dq0,j}, i^{+-}_{o,dq0,j}$ using the coordinate transformation, $T(t)$, in (12). The blocks, SD, denote the signal delay block where a delay τ is applied as in (12). Note that the delay block, SD, can be implemented in RTDS using the in-built "Variable Delay Block", which by taking $\tau = 1/(4f)$ as input allows the transformation (12) to continuously adapt to frequency changes. Since the transformer delta-side traps the zero component and improving power quality is of utmost importance, only the positive and negative components, $i^{+-}_{dq,j}, v^{+-}_{o,dq,j}, i^{+-}_{o,dq,j}$, are used in the control design. These are obtained by passing $i^{+-}_{dq0,j}, v^{+-}_{o,dq0,j}, i^{+-}_{o,dq0,j}$ through signal selectors, denoted by blocks SLT in Fig. 1. The controllers featured in the grid-forming control are presented in Sections III-A–III-C, and their satisfaction of **S1**–**S5** is highlighted in Section III-D.

A. Frequency and Voltage Droop Control

Grid-forming inverters, unlike grid-following control, are required to set and regulate the frequency and voltage of the grid they form in a synchronized manner. Beyond enabling this functionality in balanced scenarios, the UNIFI specifications [33] demand grid-forming inverters to set and regulate frequency and voltage under unbalanced conditions and facilitate active power sharing among multiple interconnected inverters. The aim is to design a frequency and voltage control that satisfies these specifications.

To this end, a frequency and voltage droop control enhanced with current limiting capability, $\mu_j \in \mathbb{R}_{>0}$ (designed in Section III-C), is proposed, as follows

$$\omega_j = \omega_{\text{ref}} - \mu_j\,k_{p,j}\,P_{0,j} \tag{30a}$$

$$V_j = V_{\text{ref}} - \mu_j\,k_{q,j}\,Q_{0,j} \tag{30b}$$

where $\omega_{\text{ref}}, V_{\text{ref}} \in \mathbb{R}_{>0}$ are the reference (nominal) frequency and voltage amplitude, respectively, and $\omega_j, V_j \in \mathbb{R}$ are the frequency and voltage, respectively. The droop gains, $k_{p,j}, k_{q,j} \in \mathbb{R}_{>0}$, can be chosen in proportion to the inverter ratings. Recall in (27)–(28) that active and reactive power oscillate at twice the system frequency under unbalanced conditions. To improve power quality delivery, active and reactive power, $P_{0.j}, Q_{0,j} \in \mathbb{R}$, corresponding to the constant terms, avg_P and avg_Q in (27)–(28), are used in (30), as follows

$$\begin{aligned} P_{0,j} &:= avg_P = v^{+\top}_{o,dq,j}\,i^{+}_{o,dq,j} + v^{-\top}_{o,dq,j}\,i^{-}_{o,dq,j} \\ Q_{0,j} &:= avg_Q = v^{+\top}_{o,dq,j}J^{\top}i^{+}_{o,dq,j} + v^{-\top}_{o,dq,j}J^{\top}i^{-}_{o,dq,j}. \end{aligned} \tag{31}$$

The use of the non-oscillating power, $P_{0,j}, Q_{0,j} \in \mathbb{R}$, improves power quality and eliminates the need for low-pass filters, which would otherwise be necessary if the oscillating power (27)–(28) were used.

In contrast to existing droop control [7]–[11], the proposed control (30) integrates a current limiting feature, μ_j. To show its benefit, it is well known that small droop gains, $k_{p,j}, k_{q,j}$, improve stability [7]. Since μ_j is designed to take values in the range $0 < \mu_j < 1$ (refer to (36)) under faulty conditions, this effectively reduces the values of $\mu_j\,k_{p,j}, \mu_j\,k_{q,j}$ in (30), thereby improving stability during abnormal conditions. Further discussions on how (30) satisfies **S1**–**S2** are given in Section III-D.

B. Voltage and Current Control Loops

According to UNIFI specifications [33], grid-forming inverters should be able to regulate the voltage of the grid they form under unbalanced conditions. Achieving this requires the generation of the modulating signal, $m_{abc,j}(t)$, such that the inverter output voltage tracks the voltage amplitude, V_j, in (30b).

Therefore, a nested voltage and current control loop enhanced with current limiting capability, $\mu_j \in \mathbb{R}_{>0}$ (designed in Section III-C), is proposed, as follows

$$\begin{aligned} \dot{\eta}^{+-}_{dq,j} &= v^{+-}_{o,dq,j} - \mathbf{e}_1 V_j \\ i^{\text{ref}+-}_{dq,j} &= -K_{\text{PV},j}(v^{+-}_{o,dq,j} - \mathbf{e}_1 V_j) - K_{\text{IV},j}\eta^{+-}_{dq,j} \end{aligned} \tag{32}$$

$$\begin{aligned} \dot{\zeta}^{+-}_{dq,j} &= i^{+-}_{dq,j} - \mu_j\,i^{\text{ref}+-}_{dq,j} \\ m^{+-}_{dq,j} &= -K_{\text{PC},j}(i^{+-}_{dq,j} - \mu_j\,i^{\text{ref}+-}_{dq,j}) - K_{\text{IC},j}\,\zeta^{+-}_{dq,j}, \end{aligned} \tag{33}$$

where (32)–(33) describe the voltage and current control loops, respectively, with integrator states, $\eta^{+-}_{dq,j}, \zeta^{+-}_{dq,j}$, and proportional $K_{\text{PV},j}, K_{\text{PC},j} \in \mathbb{R}_{>0}$ and integrals $K_{\text{IV},j}, K_{\text{IC},j} \in \mathbb{R}_{\geq 0}$ gains; and $\mathbf{e}_1 \in \mathbb{R}^4$. In (32), the inverter output voltage tracks the voltage setpoint, V_j, by generating the reference current, $i^{\text{ref}+-}_{dq,j}$, which is produced by means of proportional-integral control on the voltage deviation, $v^{+-}_{o,dq,j} - \mathbf{e}_1 V_j$. Then the inverter modulating signal, $m^{+-}_{dq,j}$, is generated by means of proportional-integral control on the current deviation, $i^{+-}_{dq,j} - \mu\,i^{\text{ref}+-}_{dq,j}$. Finally, the modulating signal, $m_{abc,j}(t)$, is obtained as follows. First, augment $m^{+-}_{dq,j}$ with the zero components $m^{+-}_{0,j}$ (chosen as zeros in this case) via a signal augmentation block denoted by AUG in Fig. 1 to obtain $m^{+-}_{dq0,j}$ (i.e., $m^{+-}_{dq0,j}(t)$). Then, using the inverse coordinate transformation (14), (15), the modulating signal, $m_{abc,j}(t)$, can be obtained by performing

$$m_{abc,j}(t) = \mathcal{U}\begin{bmatrix} m_{abc,j}(t) \\ m_{abc,j}(t-\tau) \end{bmatrix} = \mathcal{U}\,T^{-1}(t)\,m^{+-}_{dq0,j}(t) \tag{34}$$

where $\mathcal{U} = \begin{bmatrix} \mathbf{I}_3 & \mathbf{0}_{3\times 3} \\ \mathbf{0}_{3\times 3} & \mathbf{0}_{3\times 3} \end{bmatrix}$, or by directly executing

$$m_{abc,j}(t) = \mathcal{T}_t(t)\,m^{+-}_{dq0,j}(t) \tag{35}$$

which is the choice in Fig. 1, where $\mathcal{T}_t(t)$ is as in (22).

The proposed scheme (32)–(33) does not require the use

of low-pass filters as in DDSRF approaches [3, 15]–[17]. It incorporates a current limiting feature, μ_j, as opposed to existing voltage/current control loops [3, 7, 8, 15]–[17]. Also it has a simple implementation, unlike [15, 16, 18, 32]. Further discussions about (32)–(33) satisfying **S1**, **S3**–**S5** are given in Section III-D.

C. Current Limiter Design

Another UNIFI specification [33] for grid-forming inverters is fault ride-through. This is achieved through the design of μ_j which aims to protect inverters by maintaining the reference current, $i_{dq,j}^{\text{ref}+-}$ (in (33)–(32)), within acceptable range and reducing the impact of droop gains, $k_{p,j}, k_{q,j}$ (in (30)) during faulty conditions. Therefore, μ_j is designed as follows

$$\mu_j = \begin{cases} 1 & \text{if } \ \|i_{abc,j}^{\text{pk}}\|_\infty \le I_{\text{th}} \\ 1/\sigma_j & \text{if } \|i_{abc,j}^{\text{pk}}\|_\infty \ge \sigma_j I_{\text{th}}, \quad \sigma_j > 0 \\ I_{\text{th}}/\|i_{abc,j}^{\text{pk}}\|_\infty & \text{if otherwise} \end{cases} \tag{36}$$

where $\|i_{abc,j}^{\text{pk}}\|_\infty = \sqrt{2}\max\{i_{abc,j}^{\text{rms}}\}$ is the maximum of the peak values of inverter current $i_{abc,j}$ across the abc phases, and $i_{abc,j}^{\text{rms}}$ are the RMS values of $i_{abc,j}$ across the abc phases. $I_{\text{th}} \in \mathbb{R}_{>0}$ is the overcurrent threshold beyond which current restriction is initiated. The scaling factor, $\sigma_j \in \mathbb{R}_{>0}$, can be chosen based on the overcurrent rating of the inverter, so that $\sigma_j I_{\text{th}}$ gives the maximum allowable overcurrent. Unlike the current limiter in [14], the proposed current limiter (36) imposes the lower bound $1/\sigma_j$ during excessive overcurrents. This prevents assigning too small values of $I_{\text{th}}/\|i_{abc,j}^{\text{pk}}\|_\infty$ to μ_j, which can hamper the flow of current, $i_{abc,j}$, necessary to maintain stability during faulty conditions. Contrary to [22, 23], (36) avoids clipping excess current which can cause integrator wind-up, but scales it by μ_j.

Remark 1: The proposed control (30)–(33) remains stable for current limiter parameter values in $1/\sigma \le \mu_j \le 1$, $\sigma = 1.8$, as shown by the stability results in Section IV-C. I_{th} would be chosen such that the inverters can contribute to fault current for adequate sensing.

D. Satisfying Specifications *S1*–*S5*

S1: The droop control (30) satisfies **S1** by maintaining $\omega_{\text{ref}} - \mu_j\, k_{p,j}\, P_{0,j} > 0$ and $V_{\text{ref}} - \mu\, k_{q,j}\, Q_{0,j} > 0$. This is achieved by choosing the droop gains, $k_{p,j}, k_{q,j}$, sufficiently small, e.g., in the range $10^{-3}/S_{\text{rated}}$ to $10^{-2}/S_{\text{rated}}$, where S_{rated} is the inverter rating. The voltage regulation being enforced by the voltage and current control loops (32)–(33) also contributes to satisfying **S1**.

S2: The frequency control (30a) facilitates active power sharing, **S2**. To show this, consider Proposition 1 and the proof in Appendix IV.

Proposition 1: Consider a network (e.g., Fig. 2) with interconnected grid-forming inverters where each inverter uses the frequency droop control (30a) together with (30b), (32)–(33). For any inverter pair connected at buses j and k, if equilibrium is reached where the inverters synchronize, then the active power of the inverters satisfy

$$\frac{P_{0,j}^*}{P_{0,k}^*} = \frac{\mu_k}{\mu_j}\frac{k_{p,k}}{k_{p,j}} \tag{37}$$

where $P_{0,j}^*, P_{0,k}^*$ are the active powers at equilibrium.

The relation (37) shows that active power is shared among inverters according to the ratio $\mu_k\, k_{p,k}/\mu_j\, k_{p,j}$. This describes the active power sharing during abnormal conditions where the current limiting is activated with $\mu_k \neq \mu_j$. During normal operations where current is within limit, $\mu_k = \mu_j = 1$ and the active power sharing relation (37) is determined by the ratio $k_{p,k}/k_{p,j}$.

S3–**S4**: Provision of voltage support, **S3**, and injection of negative sequence current, **S4**, can be measured through the voltage unbalanced factor (VUF) and current unbalanced factor (IUF) given by [3, 18]

$$\text{VUF}_j = \frac{\sqrt{v_{o,d,j}^{-2} + v_{o,q,j}^{-2}}}{\sqrt{v_{o,d,j}^{+2} + v_{o,q,j}^{+2}}}, \qquad \text{IUF}_j = \frac{\sqrt{i_{d,j}^{-2} + i_{q,j}^{-2}}}{\sqrt{i_{d,j}^{+2} + i_{q,j}^{+2}}}. \tag{38}$$

Under unbalanced conditions, voltage support is provided if VUF is sufficiently small and negative sequence current is injected if IUF takes some values (usually greater than VUF). **S3** can be achieved by minimizing $v_{o,dq,j}^-$ and enhancing $v_{o,dq,j}^+$. This is achieved in the voltage control loop (32) by choosing the vector, $\mathbf{e}_1 = [1\ 0\ 0\ 0]^\top$, which ensures that the positive sequence voltages, $v_{o,dq,j}^+$, in $v_{o,dq,j}^{+-}$ track $[1\ 0]^\top$, while the negative sequence voltages, $v_{o,dq,j}^-$, are regulated to zero, both by the integral action in (32). Minimizing $v_{o,dq,j}^-$ leads to the generation of the negative sequence reference currents, $i_{dq,j}^{\text{ref}-}$, which tracked by $i_{dq,j}^-$ in the current control loop (33) gives some values of IUF. This shows that the current control (33) satisfies **S4**.

S5: The design (36) maintains the current, $i_{abc,j}$, within acceptable values by scaling the reference current, $i_{dq,j}^{\text{ref}+-}$, with μ_j, thus enabling the inverter to ride-through faults and contribute to fault current. Hence, **S5** is satisfied.

Remark 2: Existing grid-forming strategies for unbalanced operations would meet the UNIFI specifications, **S1**–**S5**, if they feature controllers that perform functions similar to those incorporated in the proposed control (30)–(36).

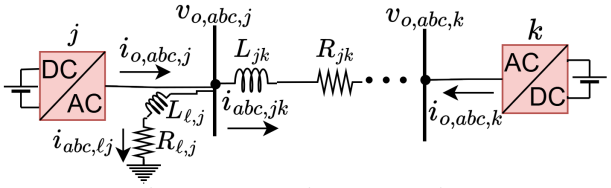

Fig. 2: Inverter interconnection.

IV. Stability Analysis

This section presents the transformation of interconnected inverters and evaluates the stability of the proposed control (30)–(36). To this end, the transformation (12) is applied to a network consisting of inverters, interconnecting lines, and loads (e.g., Fig. 2).

A. Transformation of Inverter Interconnections

We apply the coordinate transformation (12) to network systems of the form (1). To this end, recall that the transformation $T(t)$ in (7) is time dependent. The time derivative of the coordinate transformation (12) gives

$$\dot{x}^{+-}_{dq0}(t) = \dot{T}(t)\begin{bmatrix} x_{abc}(t) \\ x_{abc}(t-\tau)\end{bmatrix} + T(t)\begin{bmatrix} \dot{x}_{abc}(t) \\ \dot{x}_{abc}(t-\tau)\end{bmatrix} \quad (39a)$$

$$= \dot{T}(t)T^{-1}(t)x^{+-}_{dq0} + T(t)\begin{bmatrix} \dot{x}_{abc}(t) \\ \dot{x}_{abc}(t-\tau)\end{bmatrix} \quad (39b)$$

$$= \omega\mathcal{J}x^{+-}_{dq0} + T(t)\begin{bmatrix} \dot{x}_{abc}(t) \\ \dot{x}_{abc}(t-\tau)\end{bmatrix} \quad (39c)$$

where $\mathcal{J} = \begin{bmatrix} \tilde{J} & \mathbf{0}_{3\times3} \\ \mathbf{0}_{3\times3} & \tilde{J}^\top\end{bmatrix}$, $\tilde{J} = \begin{bmatrix} J & \mathbf{0}_2 \\ \mathbf{0}_2^\top & 0\end{bmatrix}$. Applying the transformation (39) to the inverter system (29) and neglecting the zero components gives

$$\begin{aligned} L_{f_j}\dot{i}^{+-}_{dq,j} &= (-R_{f_j}\mathbf{I}_4 + \omega_j\hat{J}L_{f_j})i^{+-}_{dq,j} + \frac{1}{2}v_{dc,j}m^{+-}_{dq,j} - v^{+-}_{o,dq,j} \\ C_{f_j}\dot{v}^{+-}_{o,dq,j} &= \omega_j C_{f_j}\hat{J}v^{+-}_{o,dq,j} + i^{+-}_{dq,j} - i^{+-}_{o,dq,j} \end{aligned} \quad (40)$$

where $\hat{J} = \begin{bmatrix} J & \mathbf{0}_{2\times2} \\ \mathbf{0}_{2\times2} & J^\top\end{bmatrix}$. Furthermore, we model the interconnection of multiple inverters and loads (e.g., Fig. 2). To do this, note that each inverter (40) has been modeled in its dq reference frame, rotating with frequency, ω_j. Since the lines interconnect multiple inverters, it is convenient to model the interconnection on a common dq reference frame, rotating with a common frequency[3] ω_s. We denote the common dq reference frame by DQ. Let $T_s(t)$ denote $T(t)$ with θ_s used in (9), where $\dot{\theta}_s = \omega_s$. Expressing (39) in the DQ reference frame yields

$$\dot{x}^{+-}_{DQ0}(t) = \omega_s\mathcal{J}x^{+-}_{DQ0} + T_s(t)\begin{bmatrix} \dot{x}_{abc}(t) \\ \dot{x}_{abc}(t-\tau)\end{bmatrix}. \quad (41)$$

Also, using $T_s(t)$ in place of $T(t)$ in (12), the coordinate transformation (12) in the DQ reference frame, with the zero components ignored, gives

$$x^{+-}_{DQ} = \mathcal{P}(\delta)x^{+-}_{dq} \quad (42)$$

where $\mathcal{P}(\delta) = \begin{bmatrix} \tilde{\mathcal{R}}(-\delta) & \mathbf{0}_{2\times2} \\ \mathbf{0}_{2\times2} & \tilde{\mathcal{R}}(\delta)\end{bmatrix}$, $\tilde{\mathcal{R}}(\cdot) = \begin{bmatrix} \cos(\cdot) & \sin(\cdot) \\ -\sin(\cdot) & \cos(\cdot)\end{bmatrix}$ and $\dot{\delta} = \omega - \omega_s$. Applying the transformation (41)-(42) to the fundamental abc equations of the passive components of lines and loads (e.g., [7]), with the zero components ignored, gives

$$\dot{\delta}_j = \omega_j - \omega_s, \quad \dot{\delta}_k = \omega_k - \omega_s \quad (43a)$$

$$\begin{aligned} L_{jk}\dot{i}^{+-}_{DQ,jk} &= (-R_{jk}\mathbf{I}_4 + \omega_s L_{jk}\hat{J})i^{+-}_{DQ,jk} + \mathcal{P}(\delta_j)v^{+-}_{o,dq,j} \\ &\quad - \mathcal{P}(\delta_k)v^{+-}_{o,dq,k} \end{aligned} \quad (43b)$$

$$\dot{i}^{+-}_{DQ,\ell j} = (-A_{\ell j} + \omega_s\hat{J})i^{+-}_{DQ,\ell j} + B_{\ell,j}\mathcal{P}(\delta_j)v^{+-}_{o,dq,j} \quad (43c)$$

$$\mathcal{P}(\delta_j)i^{+-}_{o,dq,j} = i^{+-}_{DQ,\ell j} + \sum_{\forall k\in n_j} i^{+-}_{DQ,jk} \quad (43d)$$

where (43b) describes the line connecting buses j and k, (43c) is the load at bus j, (43a) is the phase difference between the dq and DQ reference frames, and (43d) gives the total current injection at bus j. n_j denotes set of buses connected to bus j. $L_{jk}, R_{jk} \in \mathbb{R}_{>0}$ are the line inductance and resistance, respectively, where L_{jk} may also account for the coupling inductance, Lg. $i^{+-}_{DQ,jk}, i^{+-}_{DQ,\ell j} \in \mathbb{R}^4$ are the line and load currents, respectively. $A_{\ell,j}, B_{\ell,j} \in \mathbb{R}^{4\times4}$ are, respectively, matrices $T_s(\mathbf{I}_2 \otimes R_{\ell,j})(\mathbf{I}_2 \otimes L_{\ell,j})^{-1}_{\ell,j}T_s^{-1}$ and $T_s(\mathbf{I}_2 \otimes L_{\ell,j})^{-1}T_s^{-1}$ with rows and columns for the zero components eliminated, where $R_{\ell,j} = \text{diag}(R_{a,j}, R_{b,j}, R_{c,j})$, $L_{\ell,j} = \text{diag}(L_{a,j}, L_{b,j}, L_{c,j})$ are the three-phase unbalanced active and reactive components. The entries of $A_{\ell,j}, B_{\ell,j}$ are constants and independent of θ_s.

B. Generic Nonlinear Model for Inverter Interconnections

Let n, m denote the number of buses and lines, respectively, and $\mathcal{B} \in \mathbb{R}^{n\times m}$ the incidence matrix. Defining $\omega = \text{col}(\omega_j)$, $V = \text{col}(V_j)$, $\delta = \text{col}(\delta_j)$, $P_0 = \text{col}(P_{0,j})$, $Q_0 = \text{col}(Q_{0,j}) \in \mathbb{R}^n$, $i^{+-}_{o,dq} = \text{col}(v^{+-}_{o,dq,j})$, $v^{+-}_{o,dq} = \text{col}(v^{+-}_{o,dq,j})$, $i^{+-}_{DQ,\ell} = \text{col}(i^{+-}_{DQ,\ell j})$, $\eta^{+-}_{dq} = \text{col}(\eta^{+-}_{dq,j})$, $\zeta^{+-}_{dq} = \text{col}(\zeta^{+-}_{dq,j})$, $i^{\text{ref}+-}_{dq} = \text{col}(i^{\text{ref}+-}_{dq,j})$, $m^{+-}_{dq} = \text{col}(m^{+-}_{dq,j})$, $i^{+-}_{DQ,\ell} = \text{col}(i^{+-}_{DQ,\ell j}) \in \mathbb{R}^{4n}$, $i^{+-}_{DQ,L} = \text{col}(i^{+-}_{DQ,jk}) \in \mathbb{R}^{4m}$. The generic nonlinear model is given by (44)–(45) where (44) is (30)–(36), (40) for n inverters, and (45) is (43) for any network size.

$$\begin{aligned} (\mathbf{I}_n \otimes L_{f_j}\mathbf{I}_4)\dot{i}^{+-}_{dq} &= (\mathbf{I}_n \otimes (-R_{f_j}\mathbf{I}_4 + \omega_j\hat{J}L_{f_j}))i^{+-}_{dq} \\ &\quad + \frac{1}{2}(\mathbf{I}_n \otimes v_{dc,j}\mathbf{I}_4)m^{+-}_{dq} - v^{+-}_{o,dq} \\ (\mathbf{I}_n \otimes C_{f_j}\mathbf{I}_4)\dot{v}^{+-}_{o,dq} &= (\mathbf{I}_n \otimes \omega_j C_{f_j}\hat{J})v^{+-}_{o,dq} + i^{+-}_{dq} - i^{+-}_{o,dq} \\ \omega &= \omega_{\text{ref}}\mathbf{1}_n - (\mathbf{I}_n \otimes \mu_j k_{p,j})P_0 \\ V &= V_{\text{ref}}\mathbf{1}_n - (\mathbf{I}_n \otimes \mu_j k_{p,j})Q_0 \\ P_0 &= (\mathbf{I}_n \otimes v^{+-\top}_{o,dq,j})i^{+-}_{o,dq} \\ Q_0 &= (\mathbf{I}_n \otimes v^{+-\top}_{o,dq,j})(\mathbf{I}_{2n} \otimes J^\top)i^{+-}_{o,dq} \\ \dot{\eta}^{+-}_{dq} &= v^{+-}_{o,dq} - (\mathbf{I}_n \otimes \mathbf{e}_1)V \\ i^{\text{ref}+-}_{dq} &= -(\mathbf{I}_n \otimes K_{\text{PV},j}\mathbf{I}_4)(v^{+-}_{o,dq} - (\mathbf{I}_n \otimes \mathbf{e}_1)V) \\ &\quad - (\mathbf{I}_n \otimes K_{\text{IV},j}\mathbf{I}_4)\eta^{+-}_{dq} \\ \dot{\zeta}^{+-}_{dq} &= i^{+-}_{dq} - (\mathbf{I}_n \otimes \mu_j\mathbf{I}_4)i^{\text{ref}+-}_{dq} \\ m^{+-}_{dq} &= -(\mathbf{I}_n \otimes K_{\text{PC},j}\mathbf{I}_4)\Big(i^{+-}_{dq} \\ &\quad -(\mathbf{I}_n \otimes \mu_j\mathbf{I}_4)i^{\text{ref}+-}_{dq}\Big) - (\mathbf{I}_n \otimes K_{\text{IC},j}\mathbf{I}_4)\zeta^{+-}_{dq} \end{aligned} \quad (44)$$

$$\begin{aligned} \dot{\delta} &= \omega - \omega_s\mathbf{1}_n \\ (\mathbf{I}_m \otimes L_{jk}\mathbf{I}_4)\dot{i}^{+-}_{DQ,L} &= (\mathbf{I}_m \otimes (-R_{jk}\mathbf{I}_4 + \omega_s L_{jk}\hat{J}))i^{+-}_{DQ,L} \\ &\quad + (\mathcal{B}^\top \otimes \mathbf{I}_4)(\mathbf{I}_n \otimes \mathcal{P}(\delta_j))v^{+-}_{o,dq} \\ \dot{i}^{+-}_{DQ,\ell} &= (\mathbf{I}_n \otimes (-A_{\ell j} + \omega_s\hat{J}))i^{+-}_{DQ,\ell} \\ &\quad + (\mathbf{I}_n \otimes B_{\ell,j}\mathcal{P}(\delta_j))v^{+-}_{o,dq} \end{aligned} \quad (45)$$

[3] ω_s can be the synchronous frequency or the frequency of an inverter.

$$(\mathbf{I}_n \otimes \mathcal{P}(\delta_j))i^{+-}_{o,dq} = i^{+-}_{DQ,\ell} + (\mathcal{B} \otimes \mathbf{I}_4)i^{+-}_{DQ,L}$$

C. Small-Signal Stability Analysis

This section investigates the stability of the proposed control through small-signal analysis. Note that system (44)–(45) is delay-free, allowing stability assessments like eigenvalues analysis to be performed. To that end, the nonlinear system (44)–(45) with state, $z = (i^{+-}_{dq}, v^{+-}_{o,dq}, \eta^{+-}_{dq}, \zeta^{+-}_{dq}, \delta, i^{+-}_{DQ,L}, i^{+-}_{DQ,\ell})$, is linearized around an operating point, z^*. Let $\tilde{z} = z - z^*$ be the error state, the linearized model of (44)–(45) is given by

$$\dot{\tilde{z}} = \mathcal{A}\tilde{z} \tag{46}$$

where $\mathcal{A}$ is the Jacobian of (44)–(45) around $z = z^*$, with equilibrium values given in Appendix V. $\mathcal{A}$ can be extracted by straightforward calculations from (44)–(45), but is omitted here due to page constraints.

Stability analysis is performed on a three-inverter system interconnected by line impedances corresponding to the Thevenin equivalents, which are observed from each inverter side in the IEEE 123 distribution test system (Fig. 4). To facilitate controller parameter selections, eigenvalue analysis is performed. The closed-loop dominant poles loci of $\mathcal{A}$ are indicated by the red color plots (Fig. 3). The vertical black line shows the stability boundary, points $z1$ and $z2$ mark where instability occurs, while $a1$ (Fig. 3(a)) marks the oscillatory modes, which are the poles on the stability boundary imaginary axis. The movement of the poles as control parameters change from the smallest to largest values are indicated by the red color arrows. For control parameters in the range

$$\begin{aligned} &0.2 \le K_{\text{PV},j} < 0.4,\ 2 \le K_{\text{IV},j} < 8.44, \\ &0.09 \le K_{\text{PC},j} < 0.38, 0 \le K_{\text{IC},j} < 3 \times 10^{-5}, \\ &1/\sigma \le \mu_j \le 1, \sigma = 1.8, \end{aligned} \tag{47}$$

Figs. 3(a)–(b) show that the system is stable if

$$\begin{aligned} 7 \times 10^{-5} \le k_{p,j} < 1.29 \times 10^{-1}, \\ 7 \times 10^{-5} \le k_{q,j} < 3.65 \times 10^{-3}. \end{aligned} \tag{48}$$

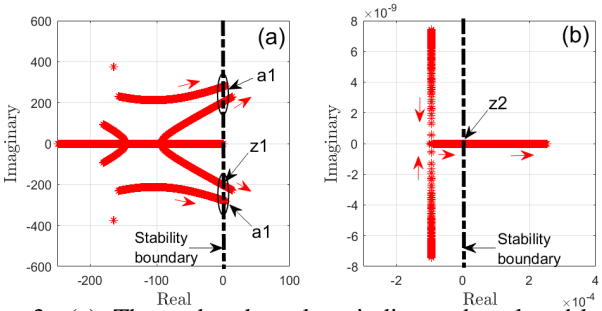

Fig. 3: (a) The red color plots indicate the closed-loop dominant poles for $7.35 \times 10^{-5} \le k_{p,j} \le 1.29 \times 10^{-1}$; (b) The red color plots indicate the closed-loop dominant poles for $7.3 \times 10^{-5} \le k_{q,j} \le 3.65 \times 10^{-3}$. $a1$ marks the oscillatory modes at $\pm j200$ and $\pm j300$, respectively.

Note that the RTDS in-built "Variable Delay Block" allows the delay-based transformation (12) to continuously adapt to frequency changes through the input, $\tau = 1/(4f)$, with $f = \omega/2\pi$. As a result, the delay-based transformation (12) and proposed control (30)–(36) are robust against frequency deviations. Also, the transformed system with control (44)–(45) is delay-free, enabling stability analysis through eigenvalues as above (Fig. 3). Adjusting control parameters as in (47)–(48) with fault-induced frequency changes $2\pi(59.98) \le \omega^*_j \le 2\pi(60.02)$ (Section V), the eigenvalue analysis performed yields eigen loci consistent with those above (Fig. 3). Choosing control parameters at or near the lower bound ensures robustness. The real-time simulations (Section V) further show that the delayed-based transformation and control remain effective under fault-induced frequency variations, yielding ripple-free responses and demonstrating continuous adaptation and unaffected performance.

Remark 3: Ensuring system's synchronous stability after disturbances is important. This can be achieved by selecting control parameters at or near the lower bound of the range in (47)–(48). This keeps the closed-loop dominant poles well left of the stability boundary, enhancing robustness. Section V follows this guideline for parameter selection.

Remark 4: We note that the stability analysis performed above (Fig. 3) is scalable, which is achieved by considering the Thevenin equivalence of the larger IEEE 123 distribution network. To that end, we have assessed the stability of a three-inverter system interconnected by line impedances corresponding to the Thevenin equivalents observed from each inverter side in the 123 distribution network. This renders the result applicable to larger networks like the 123 distribution system. Scalability is also ensured by assessing stability at some other equilibrium points obtained from the larger network.

TABLE I: Inverter and controller parameters

L_f=0.5 mH, R_f=0.0038 Ω, C_f=100 μF, ω_{ref}=2π(60) rad/s,
k_{p1}=2k_{p2}=7.35 × 10^{-5}, k_{p3}=k_{p1}, k_q=7.3 × 10^{-5},
K_{PV}=0.2, K_{IV}=2, K_{PC}=0.09, K_{IC}=10^{-5},
V_{ref}=3.4 kV (4.16 $\text{kV}_{\text{LL-rms}}$), I_{th}=4 kA, σ=1.8

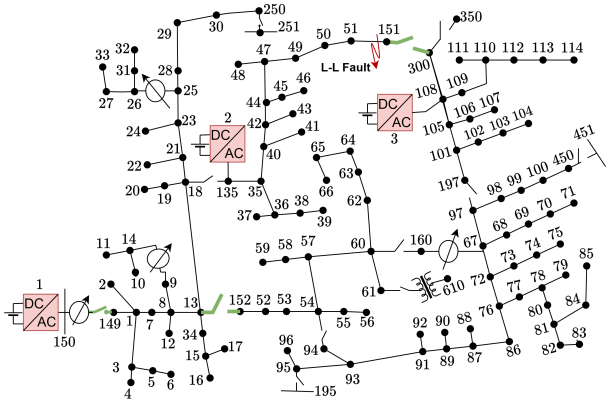

Fig. 4: IEEE 123 distribution network with three grid-forming inverters and line-to-line fault on line 51-151.

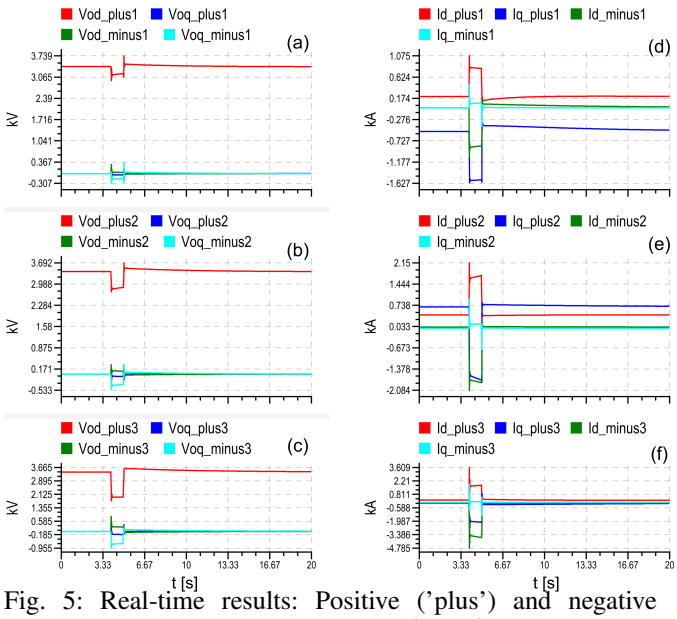

Fig. 5: Real-time results: Positive ('plus') and negative ('minus') dq voltages and currents ($v^{+-}_{o,dq}$, i^{+-}_{dq}) produced by the proposed transformation under unbalanced loading and line-to-line fault.

V. Real-Time Simulations

A. Performance of Proposed Control and Transformation

The effectiveness of the proposed control (30)–(36) and transformation (12) is validated through an EMT-based real-time simulation of a modified IEEE 123 distribution network (Fig. 4) on RTDS, with inverters 1, 2, and 3 connected at buses 150, 135, 105, along with local loads of 0.5 MW, 0.1 MW, 0.1 MW, respectively. Each inverter uses the proposed grid-forming control (30)–(36) illustrated in Fig. 1. The inverter and controller parameters are given in Table I. The control parameters are selected based on the guideline in Remark 3, which satisfies the ranges outlined in Section IV-C. The grid-forming capability of the proposed control is tested under the worst case scenario where the distribution network is isolated from the main grid.

With switches 150-149 and 151-300 closed, and switch 13-152 opened, the test is performed as follows:

- t=0-4 s (Pre-fault state): Unbalanced loading condition due to the distribution network;
- t=4-5 s (faulty state): Unbalanced loading with unbalanced line-to-line fault applied on line 51-151 at t=4 s for 60 cycles (aside imbalances and overcurrent, faults also cause phase jumps and rapid frequency changes);
- t=5-20 s (post-fault state): Fault is cleared and network returns to unbalanced loading condition due to the distribution network.

The results (Figs. 5–6) show that the network is stable and recovers to its pre-fault state after the fault is cleared. The positive and negative dq voltages and currents ($v^{+-}_{o,dq}$, i^{+-}_{dq}) for inverters 1-3 are all constant signals at steady state (Figs. 5(a)–(f)), validating the benefit of the proposed transformation (16) and confirming the results presented in (17). This is achieved without using low-pass filters (leading to fast controller response) and in the presence of unbalanced loading and fault. Also, the active and reactive power (Figs. 6), P_0, Q_0, are constant at steady state, which verifies the avg_P and avg_Q derived in (27)–(28).

Concerning specification **S1**, the inverter frequency and voltages are set and regulated despite the unbalanced loading and fault (Figs. 5(a)–(f) and 6(a), (g)). The frequencies adapt to loading and are identical at steady state, demonstrating that the inverters synchronized. The steady state frequency deviation is expected as (30a) is a primary control scheme. These demonstrate that the proposed control (30)–(36) meets frequency and voltage regulating specification, **S1**. Regarding specification **S2**, the active power shared among the inverters (Figs. 6(c)) satisfies (37), where in the pre- and post-fault μ_1=μ_2=μ_3=1 and the choices k_{p1}=2k_{p2} and k_{p3}=k_{p1} lead to active power sharing ratios $P_{0,2}/P_{0,1}$=k_{p1}/k_{p2}=2 and $P_{0,2}/P_{0,3}$=k_{p3}/k_{p2}=2 (i.e., $P_{0,2}$=2.1 MW and $P_{0,1}$=$P_{0,3}$=1.05 MW). Relation (37) also holds during the fault, in which the current limiter (36) is activated as indicated by μ_j varying within $0 < \mu_j < 1$ (Figs. 6(f)). These results show that the proposed grid-forming control (30)–(36) meets the active power sharing specification, **S2**. Furthermore, the proposed grid-forming control (30)–(36) satisfies specifications **S3**–**S4** by providing voltage support and injecting negative sequence current both during fault and unbalanced loading. This is supported by the small values of VUF compared to those of IUF (Figs. 6(b), (d)). Moreover, the current limiter (36) being activated during the fault (i.e., $0 < \mu_j < 1$ in Figs. 6(f))), indicates that the current inverter i_{abc} exceeds the threshold, I_{th}=4 kA. Thus, during fault the current, i^{pk}_{abc}, is maintained between I_{th}=4 kA and the maximum overcurrent, $I_{\max}$=7.2 kA (i.e., $I_{\max}$=σI_{th}, where σ=1.8) as shown in Figs. 6(h). Hence, the proposed grid-forming control (30)–(36) protects and enables the inverters to ride-through faults, which satisfies specification **S5**. Similar results apply with line-to-ground and three-phase-to-ground faults, which are omitted here due to page constraints. The proposed strategy being able to restore the system after faults also confirms its robustness to phase jumps and rapid frequency changes. Hence, the proposed grid-forming control (30)–(36) and transformation (12) are effective in the presence of unbalanced loading and fault and enable grid-forming capability in the distribution network. Moreover, the proposed control meets the UNIFI specifications, **S1**–**S5**, with desirable performance.

B. Comparison with Existing Control

The proposed strategy ((12), (30)–(36)) is assessed against DDSRF and PR methods, both adapted for grid-forming control by including traditional frequency/voltage droop [7] and dual control loops. While the updated DDSRF and PR satisfy criteria **S1**–**S4** under unbalanced conditions, the proposed strategy delivers superior performance meeting **S1**–**S5**. This is supported by the results in Figs. 7-8, using identical tests (as in Section V-A) and inverter and controller parameters (as in Table I). For instance, the positive and negative dq

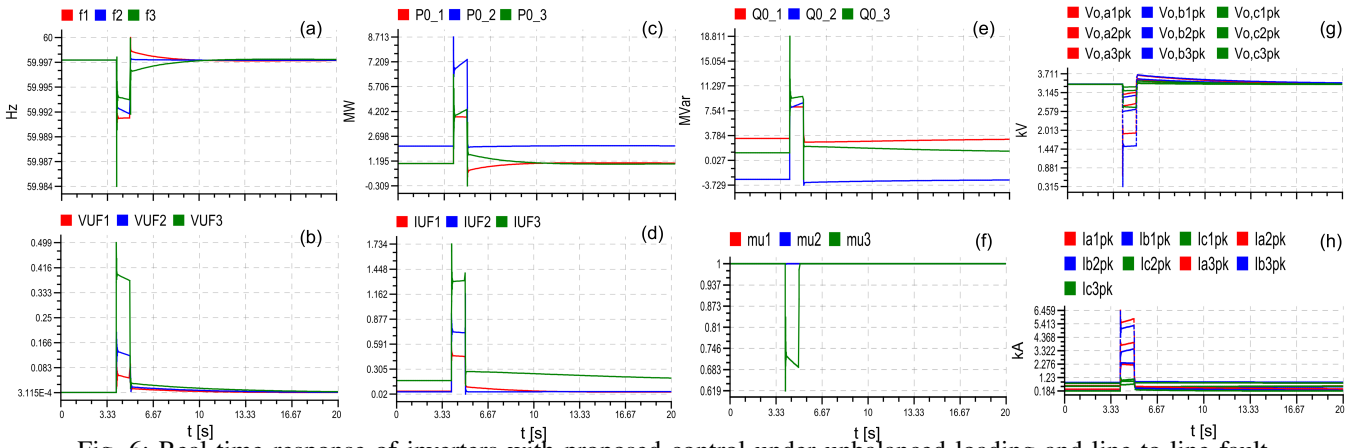

Fig. 6: Real-time response of inverters with proposed control under unbalanced loading and line-to-line fault.

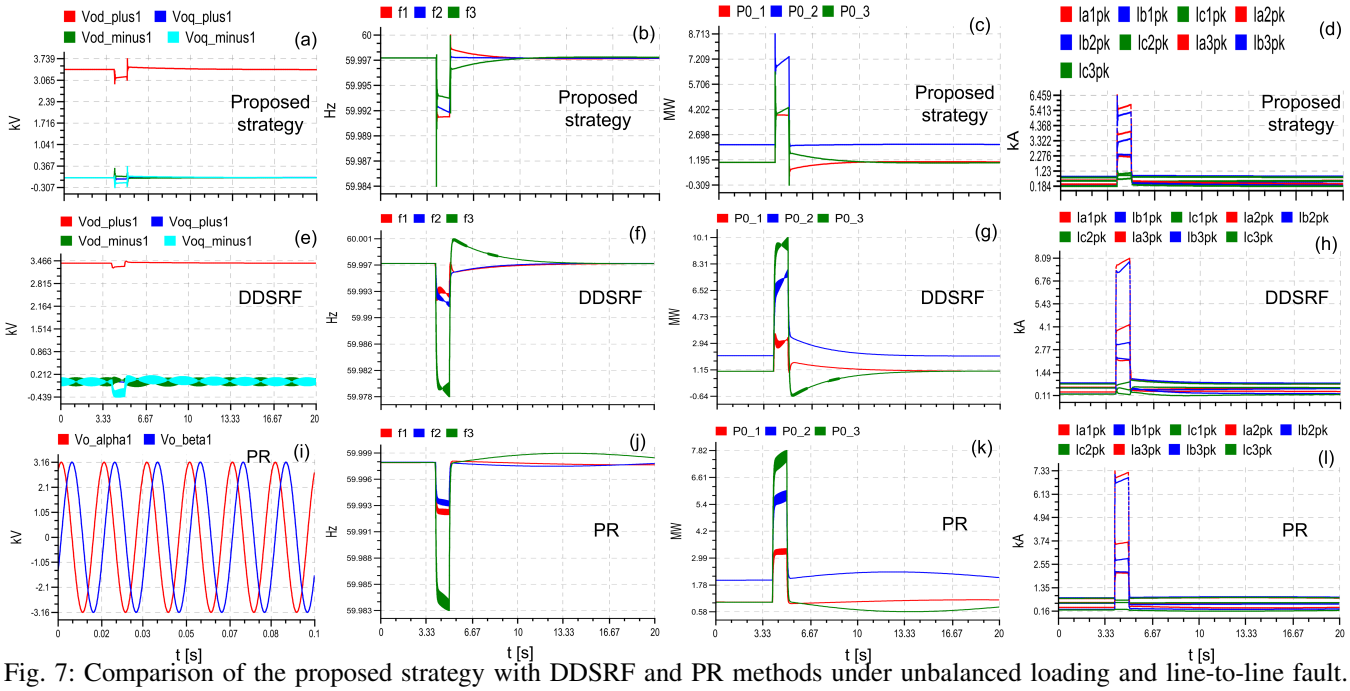

Fig. 7: Comparison of the proposed strategy with DDSRF and PR methods under unbalanced loading and line-to-line fault.

components generated by the proposed transformation are ripple-free and constant signals (Fig. 7(a)), in contrast to those obtained from DDSRF (Fig. 7(e)) which exhibit ripples despite the use of a well-tuned low-pass filters. The inverters synchronize faster with the proposed control (Fig. 7(b)) compared to DDSRF and PR controllers (Fig. 7(f), (j)). This is supported below (Table II) where for the frequency, f, the proposed strategy offers the fastest settling time (5.55 s) as against DDSRF (9.99 s) and PR ($>$ 15.54 s). Additionally, unlike DDSRF and PR (Fig. 7(g), (k)), the proposed control enables fast and ripple-free active power sharing (Fig. 7(c)). This is supported below (Table II) where for the active power, P_0, the proposed strategy has the shortest settling time (5.55 s), outperforming DDSRF (9.99 s) and PR ($>$ 15.54 s). During fault, the proposed control ensures safer fault-current ride-through (Fig. 7(d)) than DDSRF and PR (Fig. 7(h), (l)) within the allowable limits. Moreover, the responses in Fig. 8(b), (d), (f) indicates that the proposed strategy delivers faster negative current injection and voltage support (Fig. 8(a)–(b)) than both DDSRF (Fig. 8(c)–(d)) and PR (Fig. 8(e)–(f)). This is supported below (Table II) where the proposed strategy records faster settling times for IUF and VUF compared to DDSRF and PR. Furthermore, Table III shows that the proposed strategy achieves ripple-free responses in frequency, active power, IUF, and VUF, outperforming DDSRF and PR. This performance is delivered without the use of low pass filters (LPF) in the proposed strategy as opposed to DDSRF and PR. Hence, the proposed control meets the UNIFI specifications with superior performance.

VI. Conclusion

Distribution networks imbalances often cause oscillatory responses in inverter control tailored for balanced conditions. This paper has addressed the problem by developing a novel time-domain transformation suitable for inverter control and enables the conversion of three-phase unbalanced signals

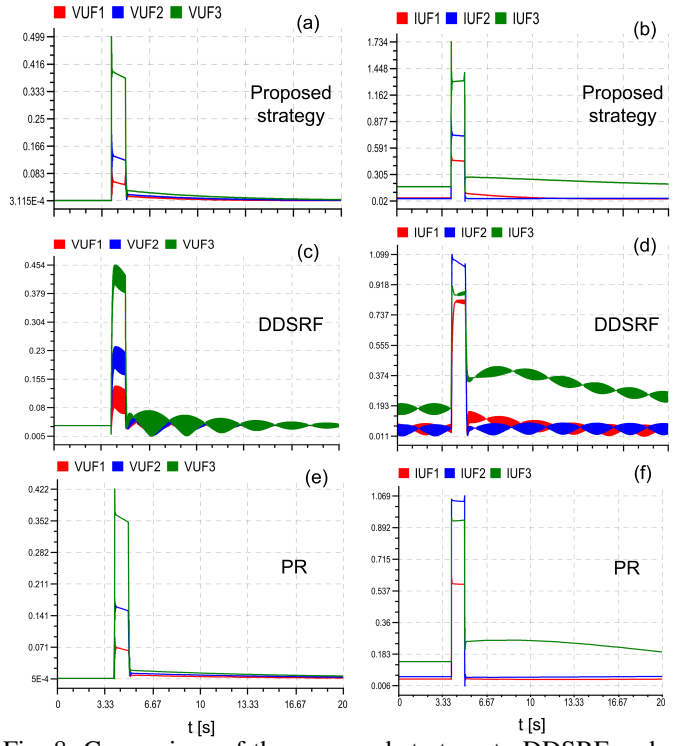

Fig. 8: Comparison of the proposed strategy to DDSRF and PR methods under unbalanced loading and line-to-line fault.

TABLE II: Settling time

	Proposed	DDSRF	PR
f	5.55 s	8.88 s	$>$ 15.54 s
P_0	5.55 s	9.99 s	$>$ 15.54 s
IUF	5.55 s	$>$ 15.54 s	$>$ 15.54 s
VUF	8.88 s	$>$ 15.54 s	8.88 s

into constant positive and negative components. Relations vital for calculating unbalanced active and reactive power have been derived from first principle and provides insight on vector products of unbalanced three-phase signals. Additionally, a grid-forming control has been developed that is effective under imbalances and delivers better performance while fulfilling UNIFI specifications. An enhanced current limiter has been designed that integrates with the proposed control featuring frequency/voltage droops and nested current and voltage control loops. Furthermore, the transformation of interconnected inverters has been presented and stability of the proposed control investigated to facilitate robust parameters selections. Analytical results and real-time simulations of a modified IEEE 123 distribution network on RTDS showed that the proposed transformation and grid-forming control are effective under imbalances. Comparison with DDSRF and PR showed that the proposed control satisfies the UNIFI requirements with a much better performance.

Appendix I
Proof of Lemma 1

Performing matrix multiplication shows that the right-hand and left-hand sides of (20a), (20c) are equal, respectively.

TABLE III: Presence of ripples

	Proposed No LPF	DDSRF LPF used	PR LPF used
f	No	Yes	Yes
P_0	No	Yes	Yes
IUF	No	Yes	No
VUF	No	Yes	No

(20b) holds noting that $\sin(-\theta) = -\sin(\theta)$ and $\cos(-\theta) = \cos(\theta)$, and (20d) holds noting that $\cos^2(\theta) + \sin^2(\theta) = 1$. (20e) holds noting that $\cos^2(\theta) - \sin^2(\theta) = \cos(2\theta)$ and $2\sin(\theta)\cos(\theta) = \sin(2\theta)$.

Appendix II
Proof of Theorem 1

To show (22), consider (10) and let

$$T_{+-0}^{-1} = \begin{bmatrix} \mathcal{T}_{11} & \mathcal{T}_{12} \\ \mathcal{T}_{21} & \mathcal{T}_{22} \end{bmatrix} \tag{49}$$

where $\mathcal{T}_{11}, \mathcal{T}_{12}, \mathcal{T}_{21}, \mathcal{T}_{22} \in \mathbb{R}^{3\times 3}$. Considering (7), performing T^{-1} gives

$$T^{-1} = \hat{T}_{\alpha\beta\gamma}^{-1} T_{+-0}^{-1} \hat{T}_{dq0}^{-1} = \hat{T}_{\alpha\beta\gamma}^{\top} T_{+-0}^{-1} \hat{T}_{dq0}^{\top} \tag{50}$$

where the second equality in (50) holds since $\hat{T}_{\alpha\beta\gamma}, \hat{T}_{dq0}$ are orthogonal matrices. Substituting for $\hat{T}_{\alpha\beta\gamma}, \hat{T}_{dq0}, T_{+-0}$ using (8), (9), (49) yields

$$\begin{aligned} T^{-1} &= \begin{bmatrix} T_{\alpha\beta\gamma}^{\top} & \mathbf{0}_{3\times 3} \\ \mathbf{0}_{3\times 3} & T_{\alpha\beta\gamma}^{\top} \end{bmatrix} \begin{bmatrix} \mathcal{T}_{11} & \mathcal{T}_{12} \\ \mathcal{T}_{21} & \mathcal{T}_{22} \end{bmatrix} \begin{bmatrix} \tilde{T}_{dq0}^{\top}(\theta) & \mathbf{0}_{3\times 3} \\ \mathbf{0}_{3\times 3} & \tilde{T}_{dq0}^{\top}(-\theta) \end{bmatrix} \\ &= \begin{bmatrix} T_{\alpha\beta\gamma}^{\top}\mathcal{T}_{11}\tilde{T}_{dq0}^{\top}(\theta) & T_{\alpha\beta\gamma}^{\top}\mathcal{T}_{12}\tilde{T}_{dq0}^{\top}(-\theta) \\ T_{\alpha\beta\gamma}^{\top}\mathcal{T}_{21}\tilde{T}_{dq0}^{\top}(\theta) & T_{\alpha\beta\gamma}^{\top}\mathcal{T}_{22}\tilde{T}_{dq0}^{\top}(-\theta) \end{bmatrix} =: \begin{bmatrix} \mathcal{T}_t \\ \mathcal{T}_\tau \end{bmatrix}, \end{aligned} \tag{51}$$

where the third equality in (51) follows from (14). Thus, the first row $\mathcal{T}_t$ corresponds to (22). To show (23), consider (22) and performing $\mathcal{T}_t^{\top}\mathcal{T}_t$ gives

$$\begin{aligned} &\mathcal{T}_t^{\top}\mathcal{T}_t \\ &= \begin{bmatrix} \tilde{T}_{dq0}(\theta)\mathcal{T}_{11}^{\top}\mathcal{T}_{11}\tilde{T}_{dq0}^{\top}(\theta) & \tilde{T}_{dq0}(\theta)\mathcal{T}_{11}^{\top}\mathcal{T}_{12}\tilde{T}_{dq0}^{\top}(-\theta) \\ \tilde{T}_{dq0}(-\theta)\mathcal{T}_{12}^{\top}\mathcal{T}_{11}\tilde{T}_{dq0}^{\top}(\theta) & \tilde{T}_{dq0}(-\theta)\mathcal{T}_{12}^{\top}\mathcal{T}_{12}\tilde{T}_{dq0}^{\top}(-\theta) \end{bmatrix} \end{aligned} \tag{52}$$

noting that $T_{\alpha\beta\gamma}$ is an orthogonal matrix. Performing T_{+-0}^{-1} shows that $\mathcal{T}_{11}, \mathcal{T}_{12}$ are as in (21) with $\mathcal{T}_{21} = \begin{bmatrix} J & \mathbf{0}_2 \\ \mathbf{0}_2^{\top} & 0 \end{bmatrix}, \mathcal{T}_{22} = \begin{bmatrix} J^{\top} & \mathbf{0}_2 \\ \mathbf{0}_2^{\top} & 2 \end{bmatrix}$. Using (21), then

$$\mathcal{T}_{11}^{\top}\mathcal{T}_{11} = \begin{bmatrix} \mathbf{I}_2 & \mathbf{0}_2 \\ \mathbf{0}_2^{\top} & 4 \end{bmatrix}, \mathcal{T}_{11}^{\top}\mathcal{T}_{12} = \mathcal{T}_{12}^{\top}\mathcal{T}_{11} = \begin{bmatrix} \mathbf{I}_2 & \mathbf{0}_2 \\ \mathbf{0}_2^{\top} & 0 \end{bmatrix}. \tag{53}$$

Using (19), (53) and the relations (20), the entries of $\mathcal{T}_t^{\top}\mathcal{T}_t$ in (52), respectively, are

$$\tilde{T}_{dq0}(\theta)\mathcal{T}_{11}^{\top}\mathcal{T}_{11}\tilde{T}_{dq0}^{\top}(\theta) = \begin{bmatrix} \mathbf{I}_2 & \mathbf{0}_2 \\ \mathbf{0}_2^{\top} & 4 \end{bmatrix} \tag{54a}$$

$$\tilde{T}_{dq0}(\theta)\mathcal{T}_{11}^{\top}\mathcal{T}_{12}\tilde{T}_{dq0}^{\top}(-\theta)=\begin{bmatrix}-\mathcal{R}(\theta)\mathcal{R}(\theta) & \mathbf{0}_2\\ \mathbf{0}_2^{\top} & 0\end{bmatrix} \tag{54b}$$

$$\tilde{T}_{dq0}(-\theta)\mathcal{T}_{12}^{\top}\mathcal{T}_{11}\tilde{T}_{dq0}^{\top}(\theta)=\begin{bmatrix}-\mathcal{R}^{\top}(\theta)\mathcal{R}^{\top}(\theta) & \mathbf{0}_2\\ \mathbf{0}_2^{\top} & 0\end{bmatrix} \tag{54c}$$

$$\tilde{T}_{dq0}(-\theta)\mathcal{T}_{12}^{\top}\mathcal{T}_{12}\tilde{T}_{dq0}^{\top}(-\theta)=\begin{bmatrix}\mathbf{I}_2 & \mathbf{0}_2\\ \mathbf{0}_2^{\top} & 0\end{bmatrix}. \tag{54d}$$

Substituting (54) into (52) gives (23). To show (24), consider (22) and performing $\mathcal{T}_t^{\top}H^{\top}\mathcal{T}_t$ gives

$$\mathcal{T}_t^{\top}H^{\top}\mathcal{T}_t=\begin{bmatrix}d_{11} & d_{12}\\ d_{21} & d_{22}\end{bmatrix} \tag{55}$$

$$\begin{aligned}
d_{11}&=\tilde{T}_{dq0}(\theta)\mathcal{T}_{11}^{\top}T_{\alpha\beta\gamma}H^{\top}T_{\alpha\beta\gamma}^{\top}\mathcal{T}_{11}\tilde{T}_{dq0}^{\top}(\theta)\\
d_{12}&=\tilde{T}_{dq0}(\theta)\mathcal{T}_{11}^{\top}T_{\alpha\beta\gamma}H^{\top}T_{\alpha\beta\gamma}^{\top}\mathcal{T}_{12}\tilde{T}_{dq0}^{\top}(-\theta)\\
d_{21}&=\tilde{T}_{dq0}(-\theta)\mathcal{T}_{12}^{\top}T_{\alpha\beta\gamma}H^{\top}T_{\alpha\beta\gamma}^{\top}\mathcal{T}_{11}\tilde{T}_{dq0}^{\top}(\theta)\\
d_{22}&=\tilde{T}_{dq0}(-\theta)\mathcal{T}_{12}^{\top}T_{\alpha\beta\gamma}H^{\top}T_{\alpha\beta\gamma}^{\top}\mathcal{T}_{12}\tilde{T}_{dq0}^{\top}(-\theta).
\end{aligned} \tag{56}$$

Using (21), then

$$\begin{aligned}
&\mathcal{T}_{11}^{\top}T_{\alpha\beta\gamma}H^{\top}T_{\alpha\beta\gamma}^{\top}\mathcal{T}_{11}=\mathcal{T}_{11}^{\top}T_{\alpha\beta\gamma}H^{\top}T_{\alpha\beta\gamma}^{\top}\mathcal{T}_{12}\\
&=\mathcal{T}_{12}^{\top}T_{\alpha\beta\gamma}H^{\top}T_{\alpha\beta\gamma}^{\top}\mathcal{T}_{11}=\mathcal{T}_{12}^{\top}T_{\alpha\beta\gamma}H^{\top}T_{\alpha\beta\gamma}^{\top}\mathcal{T}_{12}\\
&=T_{\alpha\beta\gamma}H^{\top}T_{\alpha\beta\gamma}^{\top}=\begin{bmatrix}\sqrt{3}J^{\top} & \mathbf{0}_2\\ \mathbf{0}_2^{\top} & 0\end{bmatrix}
\end{aligned} \tag{57}$$

where the last equality follows from (20a). Substituting (19) and (57) into (56) and using the properties (20) gives

$$\begin{aligned}
d_{11}&=\tilde{T}_{dq0}(\theta)\begin{bmatrix}\sqrt{3}J^{\top} & \mathbf{0}_2\\ \mathbf{0}_2^{\top} & 0\end{bmatrix}\tilde{T}_{dq0}^{\top}(\theta)=\begin{bmatrix}\sqrt{3}J^{\top} & \mathbf{0}_2\\ \mathbf{0}_2^{\top} & 0\end{bmatrix},\\
d_{12}&=\tilde{T}_{dq0}(\theta)\begin{bmatrix}\sqrt{3}J^{\top} & \mathbf{0}_2\\ \mathbf{0}_2^{\top} & 0\end{bmatrix}\tilde{T}_{dq0}^{\top}(-\theta)\\
&=\begin{bmatrix}-\sqrt{3}J^{\top}\mathcal{R}(\theta)\mathcal{R}(\theta) & \mathbf{0}_2\\ \mathbf{0}_2^{\top} & 0\end{bmatrix},\\
d_{21}&=\tilde{T}_{dq0}(-\theta)\begin{bmatrix}\sqrt{3}J^{\top} & \mathbf{0}_2\\ \mathbf{0}_2^{\top} & 0\end{bmatrix}\tilde{T}_{dq0}^{\top}(\theta)\\
&=\begin{bmatrix}-\sqrt{3}J^{\top}\mathcal{R}^{\top}(\theta)\mathcal{R}^{\top}(\theta) & \mathbf{0}_2\\ \mathbf{0}_2^{\top} & 0\end{bmatrix},\\
d_{22}&=\tilde{T}_{dq0}(-\theta)\begin{bmatrix}\sqrt{3}J^{\top} & \mathbf{0}_2\\ \mathbf{0}_2^{\top} & 0\end{bmatrix}\tilde{T}_{dq0}^{\top}(-\theta)=\begin{bmatrix}\sqrt{3}J^{\top} & \mathbf{0}_2\\ \mathbf{0}_2^{\top} & 0\end{bmatrix}.
\end{aligned}$$

Substituting for $d_{11}, d_{12}, d_{21}, d_{22}$ in (55) gives (24).

Appendix III
Proof of Theorem 2

To show (27), note that from (15) $v_{o,abc}$, $i_{o,abc}$ can, respectively, be written as $v_{o,abc}=\mathcal{T}_t\, v_{o,dq0}^{+-}$ and $i_{o,abc}=\mathcal{T}_t\, i_{o,dq0}^{+-}$. Performing $v_{o,abc}^{\top}\, i_{o,abc}$ gives

$$v_{o,abc}^{\top}\, i_{o,abc}=(\mathcal{T}_t\, v_{o,dq0}^{+-})^{\top}(\mathcal{T}_t\, i_{o,dq0}^{+-})=v_{o,dq0}^{+-\top}\mathcal{T}_t^{\top}\mathcal{T}_t\, i_{o,dq0}^{+-} \tag{58}$$

which is (25). Using (23) in Theorem 1 to substitute for $\mathcal{T}_t^{\top}\mathcal{T}_t$ in (58) gives

$$\begin{aligned}
v_{o,abc}^{\top}\, i_{o,abc}=&\, v_{o,dq}^{+\top}\, i_{o,dq}^{+}+v_{o,dq}^{-\top}\, i_{o,dq}^{-}+4v_{o,0}^{+}\, i_{o,0}^{+}\\
&-v_{o,dq}^{+\top}\mathcal{R}(\theta)\mathcal{R}(\theta)i_{o,dq}^{-}-v_{o,dq}^{-\top}\mathcal{R}^{\top}(\theta)\mathcal{R}^{\top}(\theta)i_{o,dq}^{+}.
\end{aligned}$$

Substituting (20e) and collecting like terms yields (27). To show (28), again note that from (15) $v_{o,abc}$, $i_{o,abc}$ can be written as $v_{o,abc}=\mathcal{T}_t\, v_{o,dq0}^{+-}$ and $i_{o,abc}=\mathcal{T}_t\, i_{o,dq0}^{+-}$. Executing $\frac{1}{\sqrt{3}}v_{o,abc}^{\top}H^{\top}i_{o,abc}$ gives

$$\frac{1}{\sqrt{3}}v_{o,abc}^{\top}H^{\top}i_{o,abc}=\frac{1}{\sqrt{3}}v_{o,dq0}^{+-\top}\mathcal{T}_t^{\top}H^{\top}\mathcal{T}_t\, i_{o,dq0}^{+-} \tag{59}$$

which shows (26). Using (24) in Theorem 1 to substitute for $\mathcal{T}_t^{\top}H^{\top}\mathcal{T}_t$ in (58) yields

$$\begin{aligned}
\frac{1}{\sqrt{3}}v_{o,abc}^{\top}H^{\top}i_{o,abc}=&\, v_{o,dq}^{+\top}J^{\top}i_{o,dq}^{+}+v_{o,dq}^{-\top}J^{\top}i_{o,dq}^{-}\\
&-v_{o,dq}^{+\top}J^{\top}\mathcal{R}(\theta)\mathcal{R}(\theta)i_{o,dq}^{-}-v_{o,dq}^{-\top}J^{\top}\mathcal{R}^{\top}(\theta)\mathcal{R}^{\top}(\theta)i_{o,dq}^{+}.
\end{aligned}$$

Substituting (20e) and collecting like terms gives (28).

Appendix IV
Proof of Proposition 1

Express (30a) for inverter j and k: $\omega_j=\omega_{\text{ref}}-\mu_j\, k_{p,j}\, P_{0,j}$ and $\omega_k=\omega_{\text{ref}}-\mu_k\, k_{p,k}\, P_{0,k}$. Given that synchronization holds, then $\omega_j^*-\omega_{\text{ref}}=\omega_k^*-\omega_{\text{ref}}$, where ω_j^*,ω_k^* are the equilibrium values of ω_j,ω_k, respectively. This yields $\mu_j\, k_{p,j}\, P_{0,j}=\mu_k\, k_{p,k}\, P_{0,k}$, which is (37).

Appendix V
Equilibrium Values

$v_{dc,j}$=8.7pu, δ_j^*=-10^{-6} rad, V_j^*=3.4pu, $v_{0,dq,j}^{*+-}$=$\mathbf{e}_1 V_j^*$,
$i_{o,dq,j}^{*+-}$=$[0.24, -0.09, -0.02, -0.03]$pu,
$i_{dq,j}^{*+-}$=$[0.24, 0.04, -0.02, -0.02]$pu, $i_{\ell,DQ,j}^{*+-}$=$0.99\times i_{o,dq,j}^{*+-}$,
$2\pi(59.98)\le\omega_j^*\le 2\pi(60.02)$.

References

[1] Agency for the Cooperation of Energy Regulators. (2025) Expert panel to investigate blackout in Portugal and Spain-acer.europa.eu. [Accessed 09-05-2025]. [Online]. Available: https://www.acer.europa.eu/news/expert-panel-investigate-blackout-portugal-and-spain

[2] North American Electric Reliability Corporation. (2022) Inverter-based resource strategy - ensuring reliability of the bulk power system with increased levels of bps-connected ibrs. [Accessed 05-22-2025]. [Online]. Available: https://https://www.nerc.com/comm/Documents/NERC_IBR_Strategy.pdf

[3] R. Teodorescu, M. Liserre, and P. Rodriguez, *Grid converters for photovoltaic and wind power systems*. John Wiley & Sons, 2011.

[4] A. Askarian, J. Park, and S. Salapaka, "Enhanced grid-following (e-gfl) inverter: A unified control framework for stiff and weak grids," *IEEE Transactions on Power Electronics*, vol. 39, no. 5, pp. 5089–5107, 2024.

[5] D. Pattabiraman, R. H. Lasseter, and T. M. Jahns, "Impact of phase-locked loop control on the stability of a high inverter penetration power system," in *2019 IEEE power & energy society general meeting (PESGM)*. IEEE, 2019, pp. 1–5.

[6] B. Badrzadeh, C. Cardozo, M. Hishida, S. Shah, I. Huq, N. Modi, and A. Morton, "Grid-forming inverters: Project demonstrations and pilots," *IEEE Power and Energy Magazine*, vol. 22, no. 2, pp. 66–77, 2024.

[7] N. Pogaku, M. Prodanovic, and T. C. Green, "Modeling, analysis and testing of autonomous operation of an inverter-based microgrid," *IEEE Transactions on Power Electronics*, vol. 22, no. 2, pp. 613–625, 2007.

[8] Y. Ojo, J. D. Watson, K. Laib, and I. Lestas, "A distributed scheme for voltage and frequency control and power sharing in inverter-based microgrids," *IEEE Transactions on Control Systems Technology*, 2023.

[9] A. Tayyebi, A. Anta, and F. Dörfler, "Almost globally stable grid-forming hybrid angle control," in *2020 59th IEEE Conference on Decision and Control (CDC)*. IEEE, 2020, pp. 830–835.

[10] Y. Ojo and K. Laib, "A decentralized polytopic control design for a nonlinear grid-forming inverter model," *IEEE Transactions on Control of Network Systems*, 2024.

[11] Y. Li, Y. Gu, and T. C. Green, "Revisiting grid-forming and grid-following inverters: A duality theory," *IEEE Transactions on Power Systems*, vol. 37, no. 6, pp. 4541–4554, 2022.

[12] X. Wang, Y. W. Li, F. Blaabjerg, and P. C. Loh, "Virtual-impedance-based control for voltage-source and current-source converters," *IEEE Transactions on Power Electronics*, vol. 30, no. 12, pp. 7019–7037, 2014.

[13] J. Schiffer, D. Zonetti, R. Ortega, A. M. Stanković, T. Sezi, and J. Raisch, "A survey on modeling of microgrids—from fundamental physics to phasors and voltage sources," *Automatica*, vol. 74, pp. 135–150, 2016.

[14] N. Baeckeland, D. Venkatramanan, M. Kleemann, and S. Dhople, "Stationary-frame grid-forming inverter control architectures for unbalanced fault-current limiting," *IEEE Transactions on Energy Conversion*, vol. 37, no. 4, pp. 2813–2825, 2022.

[15] M. Reyes, P. Rodriguez, S. Vazquez, A. Luna, R. Teodorescu, and J. M. Carrasco, "Enhanced decoupled double synchronous reference frame current controller for unbalanced grid-voltage conditions," *IEEE Transactions on power electronics*, vol. 27, no. 9, pp. 3934–3943, 2012.

[16] M. Reyes, P. Rodríguez, S. Vázquez, A. Luna, J. M. Carrasco, and R. Teodorescu, "Decoupled double synchronous reference frame current controller for unbalanced grid voltage conditions," in *2012 IEEE Energy Conversion Congress and Exposition (ECCE)*. IEEE, 2012, pp. 4676–4682.

[17] J. Freytes, J. Li, G. de Préville, and M. Thouvenin, "Grid-forming control with current limitation for mmc under unbalanced fault ride-through," *IEEE Transactions on Power Delivery*, vol. 36, no. 3, pp. 1914–1916, 2021.

[18] A. G. Paspatis and G. C. Konstantopoulos, "Voltage support under grid faults with inherent current limitation for three-phase droop-controlled inverters," *Energies*, vol. 12, no. 6, p. 997, 2019.

[19] ——, "Srf-based current-limiting droop controller for three-phase grid-tied inverters," in *IECON 2018-44th Annual Conference of the IEEE Industrial Electronics Society*. IEEE, 2018, pp. 282–287.

[20] B. Popadic, B. Dumnic, D. Milicevic, V. Katic, and D. Sljivac, "Grid-connected converter control during unbalanced grid conditions based on delay signal cancellation," *International Transactions on Electrical Energy Systems*, vol. 28, no. 12, p. e2636, 2018.

[21] M. Castilla, J. Miret, Á. Borrell, J. Duarte, and A. Camacho, "Improving voltage support in islanded ac microgrids during unbalanced short-circuit faults," *IEEE Transactions on Industrial Electronics*, 2024.

[22] N. Al Awadhi and M. S. El Moursi, "A novel centralized pv power plant controller for reducing the voltage unbalance factor at transmission level interconnection," *IEEE Transactions on Energy Conversion*, vol. 32, no. 1, pp. 233–243, 2016.

[23] S. Acharya, M. S. El-Moursi, A. Al-Hinai, A. S. Al-Sumaiti, and H. H. Zeineldin, "A control strategy for voltage unbalance mitigation in an islanded microgrid considering demand side management capability," *IEEE Transactions on Smart Grid*, vol. 10, no. 3, pp. 2558–2568, 2018.

[24] B. Wittenmark, "Integrators, nonlinearities, and anti-reset windup for different control structures," in *1989 American Control Conference*. IEEE, 1989, pp. 1679–1683.

[25] E. Avdiaj, J. A. Suul, S. D'Arco, and L. Piegari, "A virtual synchronous machine-based control for eliminating dc-side power oscillations of three-phase vscs under unbalanced grid voltages," in *2021 IEEE 15th International Conference on Compatibility, Power Electronics and Power Engineering (CPE-POWERENG)*. IEEE, 2021, pp. 1–6.

[26] L. He and S. Yu, "Systematic decoupling grid-forming control for utility-scale inverter-based distributed energy resources in weak distribution grids," *IEEE Open Access Journal of Power and Energy*, vol. 11, pp. 27–39, 2024.

[27] T. Liu, X. Wang, F. Liu, K. Xin, and Y. Liu, "A current limiting method for single-loop voltage-magnitude controlled grid-forming converters during symmetrical faults," *IEEE Transactions on Power Electronics*, vol. 37, no. 4, pp. 4751–4763, 2021.

[28] C. Liu, X. Cai, R. Li, and R. Yang, "Optimal short-circuit current control of the grid-forming converter during grid fault condition," *IET Renewable Power Generation*, vol. 15, no. 10, pp. 2185–2194, 2021.

[29] J. Martínez-Turégano, S. Añó-Villalba, S. Bernal-Perez, R. Peña, and R. Blasco-Gimenez, "Small-signal stability and fault performance of mixed grid forming and grid following offshore wind power plants connected to a hvdc-diode rectifier," *IET Renewable Power Generation*, vol. 14, no. 12, pp. 2166–2175, 2020.

[30] S. S. Nudehi and D. Gross, "Grid-forming control of three-phase and single-phase converters across unbalanced transmission and distribution systems," *IEEE Transactions on Power Systems*, vol. 38, no. 6, pp. 5687–5700, 2022.

[31] R. Ghosh, N. R. Tummuru, and B. S. Rajpurohit, "A new virtual oscillator-based grid-forming controller with decoupled control over individual phases and improved performance of unbalanced fault ride-through," *IEEE Transactions on Industrial Electronics*, vol. 70, no. 12, pp. 12 465–12 474, 2023.

[32] M. Awal, M. R. K. Rachi, H. Yu, I. Husain, and S. Lukic, "Double synchronous unified virtual oscillator control for asymmetrical fault ride-through in grid-forming voltage source converters," *IEEE Transactions on Power Electronics*, vol. 38, no. 6, pp. 6759–6763, 2022.

[33] B. Kroposki, "UNIFI specifications for grid-forming inverter-based resources (v. 2)," National Renewable Energy Laboratory (NREL), Golden, CO (United States), Tech. Rep., 2024.

[34] Y. Ojo and J. Schiffer, "Towards a time-domain modeling framework for small-signal analysis of unbalanced microgrids," in *2017 IEEE Manchester PowerTech*. IEEE, 2017, pp. 1–6.

[35] Y. Zhou, P. Bauer, J. A. Ferreira, and J. Pierik, "Operation of grid-connected dfig under unbalanced grid voltage condition," *IEEE Transactions on Energy Conversion*, vol. 24, no. 1, pp. 240–246, 2009.

Yemi Ojo (Member, IEEE) received his M.Sc. (Eng.) degree in electrical engineering and renewable energy systems from the University of Leeds, Leeds, U.K., in 2016, and Ph.D. degree in engineering from the University of Cambridge, Cambridge, U.K., in 2022. He is currently a Research Engineer with the Grid Integration and Control group at Idaho National Laboratory. His research interests include control and optimization of power systems with applications to microgrids.

Soumyadeep Nag (Member, IEEE) received his Ph.D. degree in electrical engineering from Baylor University, Waco, TX, USA, in 2020. He is with the Grid Integration and Control group at Idaho National Laboratory. His research focuses on the control, operation, and planning aspects of modern power systems, while considering the impact of variable and non-dispatchable generation. He serves as the Chair of the Eastern Idaho IEEE PES Chapter.

Temitayo O. Olowu (Member, IEEE) earned his M.S. and Ph.D. degrees in Electrical Engineering from Florida International University (FIU), Miami, Florida, in 2020 and 2021, respectively. He is currently a Control Research Engineer at Idaho National Laboratory. His research interests include power systems optimization and control, integrated energy systems, and grid resiliency. He also serves as a reviewer for several IEEE Transactions journals.